Production characteristics of light nuclei, hypertritons and Ω-hypernuclei in Pb+Pb collisions at $\sqrt{s_{NN}} = 5.02$ TeV*

Rui-Qin Wang,[1,†] Xin-Lei Hou,[1] Yan-Hao Li,[1] Jun Song,[2,‡] and Feng-Lan Shao[1,§]

[1] *School of Physics and Physical Engineering, Qufu Normal University, Shandong 273165, China*
[2] *School of Physical Science and Intelligent Engineering, Jining University, Shandong 273155, China*

We extend an analytical nucleon coalescence model with hyperons to study the productions of light nuclei, hypertritons and Ω-hypernuclei in Pb+Pb collisions at $\sqrt{s_{NN}} = 5.02$ TeV. We derive the formula of the momentum distribution of two bodies coalescing into dibaryon states and that of three bodies coalescing into tribaryon states. We explain the available data of coalescence factors B_2 and B_3, transverse momentum spectra, averaged transverse momenta, yield rapidity densities and yield ratios of the deuteron, antihelium-3, antitriton and hypertriton measured by the ALICE collaboration. We give predictions of different Ω-hypernuclei $H(p\Omega^-)$, $H(n\Omega^-)$ and $H(pn\Omega^-)$. We particularly study production correlations of different light (hyper-)nuclei and find two groups of interesting observables, the averaged transverse momentum ratios of light (hyper-)nuclei to protons (hyperons) and their corresponding yield ratios. The former group exhibits a reverse hierarchy of the nucleus size, and the latter is sensitive to the nucleus production mechanism as well as the nucleus's own size.

Keywords: Light nucleus production, Hypernucleus production, The coalescence model, Relativistic heavy ion collision

I. INTRODUCTION

In ultra-relativistic heavy ion collisions, light nuclei and hypernuclei such as the deuteron (d), helium-3 (^{3}He), triton (t) and hypertriton ($^3_\Lambda$H), are a special group of observables [1–21]. They are composite clusters and their production mechanism is still under debate today. The productions of such composite objects closely relate with many fundamental issues in relativistic heavy ion community, e.g., the hadronization mechanism [1], the hadronic rescattering effect [2], the structure of the quantum chromodynamics phase diagram [3–8], the local baryon-strangeness correlation [9, 10], the system freeze-out characteristic [11–16], the hyperon-nucleon interaction [17–19] and the search of more hadronic molecular states [20, 21].

In recent decades, the productions of light nuclei and hypernuclei in ultra-relativistic heavy ion collisions have always attracted much attention both in experiment [22–35] and in theory [36–47]. The STAR experiment at the BNL Relativistic Heavy Ion Collider (RHIC) and the ALICE experiment at the CERN Large Hadron Collider (LHC) have put much effort into measurements of light nuclei [25–30] and hypernuclei [31–34]. In theory two production mechanisms, the thermal production mechanism [47–51] and the coalescence mechanism [40, 41, 52–61], have proved to be successful in describing formations of such composite objects.

The coalescence mechanism, assuming light nuclei and hypernuclei are produced by the coalescence of the jacent nucleons and hyperons in the phase space, possesses some unique characteristics [40, 41, 59–63]. To see whether, if so, to what extent, these characteristics depend on the particular coalescence models used in obtaining these characteristics, we developed an analytical method for describing productions of different species of light nuclei in our previous works [64–67]. We applied the analytical nucleon coalescence model to Au+Au collisions at the RHIC to successfully explain the energy-dependent behaviors of d, t, ^{3}He and ^{4}He [64, 65]. We also applied it to pp, p+Pb, and Pb+Pb collisions at the LHC to understand different behaviors of coalescence factors B_2 and B_3 [66] from small to large collision systems, and gave a series of concise production correlations of d, ^{3}He and t [67].

Very recently, the ALICE collaboration published the most precise measurements of d, ^{3}He, t and especially $^3_\Lambda$H in Pb+Pb collisions at $\sqrt{s_{NN}} = 5.02$ TeV to date [30, 33, 68]. In this work, we extend the coalescence model considering the coordinate-momentum correlation [67] to include the hyperon coalescence besides the nucleon coalescence and apply it to simultaneously study the productions of light nuclei, the $^3_\Lambda$H and Ω-hypernuclei. One main goal of this article is to give an overall comprehension of the newest data in Pb+Pb collisions with the highest collision energy so far. The other goal is to bring production characteristics, especially production correlations, of light nuclei and hypernuclei originating from the coalescence itself to light. We propose two groups of interesting observables, the averaged transverse momentum ratios and centrality-dependent yield ratios of light nuclei to protons and hypernuclei to hyperons. These ratios happen to offset the differences of the primordial p, Λ and Ω^-. This makes them powerful to reveal whether there exists a universal production mechanism for different species of nuclei in light and strange sectors. We find these ratios exhibit certain relations in the coalescence picture, which are very different from the thermal production mechanism.

The paper is organized as follows. In Sec. II, we introduce the coalescence model. We present the formulae of the momentum distributions of two baryons coalescing into dibaryon states and three baryons coalescing into tribaryon states, respectively. In Sec. III, we study behaviors of B_2 and B_3 as functions of the collision centrality and the transverse momentum per nucleon. We also study the transverse momen-

* Supported by the National Natural Science Foundation of China (No. 12175115 and No. 12375074)
† wangrq@qfnu.edu.cn
‡ songjun2011@jnxy.edu.cn
§ Corresponding author, shaofl@mail.sdu.edu.cn

tum (p_T) spectra, averaged transverse momenta $\langle p_T\rangle$, yield rapidity densities dN/dy and yield ratios of d, $^3\overline{\mathrm{He}}$ and $\bar{t}$. In Sec. IV, we present results of the $^3_\Lambda$H and Ω-hypernuclei. We specially study the averaged transverse momentum ratios $\frac{\langle p_T\rangle_d}{\langle p_T\rangle_p}$, $\frac{\langle p_T\rangle_{H(p\Omega^-)}}{\langle p_T\rangle_{\Omega^-}}$, $\frac{\langle p_T\rangle_{H(n\Omega^-)}}{\langle p_T\rangle_{\Omega^-}}$, $\frac{\langle p_T\rangle_t}{\langle p_T\rangle_p}$, $\frac{\langle p_T\rangle_{^3\mathrm{He}}}{\langle p_T\rangle_p}$, $\frac{\langle p_T\rangle_{^3_\Lambda\mathrm{H}}}{\langle p_T\rangle_\Lambda}$, $\frac{\langle p_T\rangle_{H(pn\Omega^-)}}{\langle p_T\rangle_{\Omega^-}}$, and centrality-dependent behaviors of yield ratios $\frac{d}{p}$, $\frac{H(p\Omega^-)}{\Omega^-}$, $\frac{H(n\Omega^-)}{\Omega^-}$, $\frac{t}{p}$, $\frac{^3\mathrm{He}}{p}$, $\frac{^3_\Lambda\mathrm{H}}{\Lambda}$, $\frac{H(pn\Omega^-)}{\Omega^-}$. In Sec. V, we give our summary.

II. THE COALESCENCE MODEL

In this section, we extend the analytical nucleon coalescence model in our previous work [67] to include the hyperon coalescence. In the current model, the coalescence process is executed on an equivalent kinetic freeze-out surface formed from different times. To make the analytical and intuitive insights possible, we abandon carrying out the time evolution step by step but absorb the finite emission duration in an effective volume. We first present the formalism of two baryons coalescing into d-like dibaryon states. We then give an analytical expression of three baryons coalescing into ^{3}He, t, and their partners in the strange sector.

A. Formalism of two bodies coalescing into dibaryon states

We begin with a hadronic system produced at the final stage of the evolution of high energy collision, and suppose the dibaryon state H_j is formed via the coalescence of two baryons h_1 and h_2. We use $f_{H_j}(\boldsymbol{p})$ to denote the three-dimensional momentum distribution of the produced H_j and it is given by

$$\begin{aligned} f_{H_j}(\boldsymbol{p}) =& \int d\boldsymbol{x}_1 d\boldsymbol{x}_2 d\boldsymbol{p}_1 d\boldsymbol{p}_2 f_{h_1h_2}(\boldsymbol{x}_1,\boldsymbol{x}_2;\boldsymbol{p}_1,\boldsymbol{p}_2) \\ &\times \mathcal{R}_{H_j}(\boldsymbol{x}_1,\boldsymbol{x}_2;\boldsymbol{p}_1,\boldsymbol{p}_2,\boldsymbol{p}). \end{aligned} \tag{1}$$

$f_{h_1h_2}(\boldsymbol{x}_1,\boldsymbol{x}_2;\boldsymbol{p}_1,\boldsymbol{p}_2)$ is the two-baryon joint coordinate-momentum distribution; $\mathcal{R}_{H_j}(\boldsymbol{x}_1,\boldsymbol{x}_2;\boldsymbol{p}_1,\boldsymbol{p}_2,\boldsymbol{p})$ is the kernel function of the H_j. Here and from now on we use bold symbols to denote three-dimensional coordinate or momentum vectors.

In terms of the normalized joint coordinate-momentum distribution denoted by the superscript '(n)', we have

$$\begin{aligned} f_{H_j}(\boldsymbol{p}) =& N_{h_1h_2} \int d\boldsymbol{x}_1 d\boldsymbol{x}_2 d\boldsymbol{p}_1 d\boldsymbol{p}_2 f^{(n)}_{h_1h_2}(\boldsymbol{x}_1,\boldsymbol{x}_2;\boldsymbol{p}_1,\boldsymbol{p}_2) \\ &\times \mathcal{R}_{H_j}(\boldsymbol{x}_1,\boldsymbol{x}_2;\boldsymbol{p}_1,\boldsymbol{p}_2,\boldsymbol{p}). \end{aligned} \tag{2}$$

$N_{h_1h_2} = N_{h_1}N_{h_2}$ is the number of all possible h_1h_2-pairs in the considered hadronic system, and N_{h_i} $(i=1,2)$ is the number of the baryons h_i.

The kernel function $\mathcal{R}_{H_j}(\boldsymbol{x}_1,\boldsymbol{x}_2;\boldsymbol{p}_1,\boldsymbol{p}_2,\boldsymbol{p})$ denotes the probability density for h_1, h_2 with momenta $\boldsymbol{p}_1$ and $\boldsymbol{p}_2$ at $\boldsymbol{x}_1$ and $\boldsymbol{x}_2$ to combine into an H_j of momentum $\boldsymbol{p}$. It carries the kinetic and dynamical information of h_1 and h_2 combining into H_j, and its precise expression should be constrained by such as the momentum conservation, and constraints due to intrinsic quantum numbers e.g., spin [64–67]. To take these constraints into account explicitly, we rewrite the kernel function in the following form

$$\begin{aligned} \mathcal{R}_{H_j}(\boldsymbol{x}_1,\boldsymbol{x}_2;\boldsymbol{p}_1,\boldsymbol{p}_2,\boldsymbol{p}) =& g_{H_j}\mathcal{R}^{(x,p)}_{H_j}(\boldsymbol{x}_1,\boldsymbol{x}_2;\boldsymbol{p}_1,\boldsymbol{p}_2) \\ &\times \delta(\sum_{i=1}^{2}\boldsymbol{p}_i - \boldsymbol{p}). \end{aligned} \tag{3}$$

The spin degeneracy factor $g_{H_j} = (2J_{H_j}+1)/[\prod_{i=1}^{2}(2J_{h_i}+1)]$, where J_{H_j} is the spin of the produced H_j and J_{h_i} is that of the primordial baryon h_i. The Dirac δ function guarantees the momentum conservation in the coalescence process. The remaining $\mathcal{R}^{(x,p)}_{H_j}(\boldsymbol{x}_1,\boldsymbol{x}_2;\boldsymbol{p}_1,\boldsymbol{p}_2)$ can be solved from the Wigner transformation as the H_j wave function is given. Considering the wave function of a spherical harmonic oscillator is particularly tractable and useful for analytical insight, we adopt this profile as in Refs. [69–71] and have

$$\mathcal{R}^{(x,p)}_{H_j}(\boldsymbol{x}_1,\boldsymbol{x}_2;\boldsymbol{p}_1,\boldsymbol{p}_2) = 8e^{-\frac{(\boldsymbol{x}'_1-\boldsymbol{x}'_2)^2}{2\sigma^2}} e^{-\frac{2\sigma^2(m_2\boldsymbol{p}'_1-m_1\boldsymbol{p}'_2)^2}{(m_1+m_2)^2}}. \tag{4}$$

The superscript '$'$' in the coordinate or momentum variables denotes the baryon coordinate or momentum in the rest frame of h_1h_2-pair. m_1 and m_2 are the mass of h_1 and that of h_2. The width parameter $\sigma = \sqrt{\frac{2(m_1+m_2)^2}{3(m_1^2+m_2^2)}}R_{H_j}$, and R_{H_j} is the root-mean-square radius of H_j.

Substituting Eqs. (3) and (4) into Eq. (2), we have

$$\begin{aligned} f_{H_j}(\boldsymbol{p}) =& N_{h_1h_2} g_{H_j} \int d\boldsymbol{x}_1 d\boldsymbol{x}_2 d\boldsymbol{p}_1 d\boldsymbol{p}_2 f^{(n)}_{h_1h_2}(\boldsymbol{x}_1,\boldsymbol{x}_2;\boldsymbol{p}_1,\boldsymbol{p}_2) \\ &\times 8e^{-\frac{(\boldsymbol{x}'_1-\boldsymbol{x}'_2)^2}{2\sigma^2}} e^{-\frac{2\sigma^2(m_2\boldsymbol{p}'_1-m_1\boldsymbol{p}'_2)^2}{(m_1+m_2)^2}} \delta(\sum_{i=1}^{2}\boldsymbol{p}_i - \boldsymbol{p}). \end{aligned} \tag{5}$$

This is the general formalism of the H_j production via the coalescence of two baryons h_1 and h_2.

Noticing that the root-mean-square radius R_{H_j} of the dibaryon state H_j is always about or larger than 2 fm, σ is even larger than R_{H_j}. So the gaussian width in the momentum-dependent part of the kernel function in Eq. (5) has a small value, about or smaller than 0.1 GeV/c. Therefore, we approximate the gaussian form of the momentum-dependent kernel function to be a δ function form as follows

$$e^{-\frac{(\boldsymbol{p}'_1-\frac{m_1}{m_2}\boldsymbol{p}'_2)^2}{(1+\frac{m_1}{m_2})^2/(2\sigma^2)}} \approx \left[\frac{\sqrt{\pi}}{\sqrt{2}\sigma}(1+\frac{m_1}{m_2})\right]^3 \delta(\boldsymbol{p}'_1 - \frac{m_1}{m_2}\boldsymbol{p}'_2). \tag{6}$$

The robustness of this δ function approximation has been checked at the outset of the analytical coalescence model in our previous work [66]. Substituting Eq. (6) into Eq. (5) and integrating $\boldsymbol{p}_1$ and $\boldsymbol{p}_2$, we can obtain

$$f_{H_j}(\boldsymbol{p}) = N_{h_1h_2} g_{H_j} \int d\boldsymbol{x}_1 d\boldsymbol{x}_2 d\boldsymbol{p}_1 d\boldsymbol{p}_2$$

$$f^{(n)}_{h_1h_2}(\boldsymbol{x}_1,\boldsymbol{x}_2;\boldsymbol{p}_1,\boldsymbol{p}_2)8e^{-\frac{(\boldsymbol{x}'_1-\boldsymbol{x}'_2)^2}{2\sigma^2}}(\frac{\sqrt{\pi}}{\sqrt{2}\sigma})^3(1+\frac{m_1}{m_2})^3$$
$$\times\delta(\boldsymbol{p}'_1-\frac{m_1}{m_2}\boldsymbol{p}'_2)\delta(\sum_{i=1}^{2}\boldsymbol{p}_i-\boldsymbol{p})$$
$$=N_{h_1h_2}g_{H_j}\int d\boldsymbol{x}_1d\boldsymbol{x}_2d\boldsymbol{p}_1d\boldsymbol{p}_2f^{(n)}_{h_1h_2}(\boldsymbol{x}_1,\boldsymbol{x}_2;\boldsymbol{p}_1,\boldsymbol{p}_2)$$
$$\times 8e^{-\frac{(\boldsymbol{x}'_1-\boldsymbol{x}'_2)^2}{2\sigma^2}}(\frac{\sqrt{\pi}}{\sqrt{2}\sigma})^3(1+\frac{m_1}{m_2})^3\gamma\delta(\boldsymbol{p}_1-\frac{m_1}{m_2}\boldsymbol{p}_2)$$
$$\times\delta(\sum_{i=1}^{2}\boldsymbol{p}_i-\boldsymbol{p})$$
$$=N_{h_1h_2}g_{H_j}\gamma(\frac{\sqrt{\pi}}{\sqrt{2}\sigma})^3\times 8\int d\boldsymbol{x}_1d\boldsymbol{x}_2$$
$$f^{(n)}_{h_1h_2}(\boldsymbol{x}_1,\boldsymbol{x}_2;\frac{m_1\boldsymbol{p}}{m_1+m_2},\frac{m_2\boldsymbol{p}}{m_1+m_2})e^{-\frac{(\boldsymbol{x}'_1-\boldsymbol{x}'_2)^2}{2\sigma^2}}. \quad (7)$$

The γ is the Lorentz contraction factor corresponding to the three-dimensional velocity $\boldsymbol{\beta}$ of the center-of-mass frame of h_1h_2-pair in the laboratory frame. Here the momentum transformation parallel to $\boldsymbol{\beta}$ is $p'_{1//}-\frac{m_1}{m_2}p'_{2//}=\frac{1}{\gamma}(p_{1//}-\frac{m_1}{m_2}p_{2//})$ and that perpendicular to $\boldsymbol{\beta}$ is invariant.

Changing coordinate variables in Eq. (7) to be $\boldsymbol{X}=\frac{m_1\boldsymbol{x}_1+m_2\boldsymbol{x}_2}{\sqrt{2}(m_1+m_2)}$ and $\boldsymbol{r}=\frac{\boldsymbol{x}_1-\boldsymbol{x}_2}{\sqrt{2}}$, we have

$$f_{H_j}(\boldsymbol{p})=N_{h_1h_2}g_{H_j}\gamma(\frac{\sqrt{\pi}}{\sqrt{2}\sigma})^3\times$$
$$8\int d\boldsymbol{X}d\boldsymbol{r}f^{(n)}_{h_1h_2}(\boldsymbol{X},\boldsymbol{r};\frac{m_1\boldsymbol{p}}{m_1+m_2},\frac{m_2\boldsymbol{p}}{m_1+m_2})e^{-\frac{\boldsymbol{r}'^2}{\sigma^2}}. \quad (8)$$

Considering the strong interaction and the coalescence are local, we neglect the effect of collective motion on the center of mass coordinate and assume it is factorized, i.e.,

$$f^{(n)}_{h_1h_2}(\boldsymbol{X},\boldsymbol{r};\frac{m_1\boldsymbol{p}}{m_1+m_2},\frac{m_2\boldsymbol{p}}{m_1+m_2})=f^{(n)}_{h_1h_2}(\boldsymbol{X})$$
$$\times f^{(n)}_{h_1h_2}(\boldsymbol{r};\frac{m_1\boldsymbol{p}}{m_1+m_2},\frac{m_2\boldsymbol{p}}{m_1+m_2}). \quad (9)$$

Substituting Eq. (9) into Eq. (8), we have

$$f_{H_j}(\boldsymbol{p})=N_{h_1h_2}g_{H_j}\gamma(\frac{\sqrt{\pi}}{\sqrt{2}\sigma})^3$$
$$\times 8\int d\boldsymbol{r}f^{(n)}_{h_1h_2}(\boldsymbol{r};\frac{m_1\boldsymbol{p}}{m_1+m_2},\frac{m_2\boldsymbol{p}}{m_1+m_2})e^{-\frac{\boldsymbol{r}'^2}{\sigma^2}}. \quad (10)$$

We adopt the frequently-used gaussian form for the relative coordinate distribution as in such as Refs. [72–74], i.e.,

$$f^{(n)}_{h_1h_2}(\boldsymbol{r};\frac{m_1\boldsymbol{p}}{m_1+m_2},\frac{m_2\boldsymbol{p}}{m_1+m_2})=\frac{1}{\left[\pi C_0R_f^2(\boldsymbol{p})\right]^{3/2}}$$
$$\times e^{-\frac{\boldsymbol{r}^2}{C_0R_f^2(\boldsymbol{p})}}f^{(n)}_{h_1h_2}(\frac{m_1\boldsymbol{p}}{m_1+m_2},\frac{m_2\boldsymbol{p}}{m_1+m_2}). \quad (11)$$

Here $R_f(\boldsymbol{p})$ is the effective radius of the hadronic source system at the H_j freeze-out. C_0 is introduced to make $\boldsymbol{r}^2/C_0$ to be the square of one-half of the relative position and it is 2 [72–74]. In this way $R_f(\boldsymbol{p})$ is just the Hanbury-Brown-Twiss (HBT) interferometry radius, which can also be extracted from the two-particle femtoscopic correlations [73, 74].

With instantaneous coalescence in the rest frame of h_1h_2-pair, i.e., $\Delta t'=0$, we get the coordinate transformation

$$\boldsymbol{r}=\boldsymbol{r}'+(\gamma-1)\frac{\boldsymbol{r}'\cdot\boldsymbol{\beta}}{\beta^2}\boldsymbol{\beta}. \quad (12)$$

The instantaneous coalescence is a basic assumption in coalescence-like models where the overlap of the nucleus Wigner phase-space density with the constituent phase-space distributions is adopted [69]. Considering the coalescence criterion judging in the rest frame is more general than in the laboratory frame, we choose the instantaneous coalescence in the rest frame of h_1h_2-pair, as in Refs. [15, 69]. Substituting Eq. (11) into Eq. (10) and using Eq. (12) to integrate from the relative coordinate variable, we obtain

$$f_{H_j}(\boldsymbol{p})=\frac{8\pi^{3/2}g_{H_j}\gamma}{2^{3/2}\left[C_0R_f^2(\boldsymbol{p})+\sigma^2\right]\sqrt{C_0[R_f(\boldsymbol{p})/\gamma]^2+\sigma^2}}$$
$$\times f_{h_1h_2}(\frac{m_1\boldsymbol{p}}{m_1+m_2},\frac{m_2\boldsymbol{p}}{m_1+m_2}). \quad (13)$$

Ignoring correlations between h_1 and h_2, we have the three-dimensional momentum distribution of the H_j as

$$f_{H_j}(\boldsymbol{p})=\frac{8\pi^{3/2}g_{H_j}\gamma}{2^{3/2}\left[C_0R_f^2(\boldsymbol{p})+\sigma^2\right]\sqrt{C_0[R_f(\boldsymbol{p})/\gamma]^2+\sigma^2}}$$
$$\times f_{h_1}(\frac{m_1\boldsymbol{p}}{m_1+m_2})f_{h_2}(\frac{m_2\boldsymbol{p}}{m_1+m_2}). \quad (14)$$

Denoting the Lorentz invariant momentum distribution $E\frac{d^3N}{d\boldsymbol{p}^3}=\frac{d^2N}{2\pi p_Tdp_Tdy}$ with $f^{(inv)}$, we finally have

$$f^{(inv)}_{H_j}(p_T,y)=\frac{8\pi^{3/2}g_{H_j}}{2^{3/2}\left[C_0R_f^2(p_T,y)+\sigma^2\right]\sqrt{C_0\frac{R_f^2(p_T,y)}{\gamma^2}+\sigma^2}}$$
$$\times\frac{m_{H_j}}{m_1m_2}f^{(inv)}_{h_1}(\frac{m_1p_T}{m_1+m_2},y)f^{(inv)}_{h_2}(\frac{m_2p_T}{m_1+m_2},y), \quad (15)$$

where y is the longitudinal rapidity and m_{H_j} is the mass of the H_j.

B. Formalism of three bodies coalescing into tribaryon states

For tribaryon state H_j formed via the coalescence of three baryons h_1, h_2 and h_3, the momentum distribution $f_{H_j}(\boldsymbol{p})$ is

$$f_{H_j}(\boldsymbol{p}) = N_{h_1h_2h_3} \int d\boldsymbol{x}_1 d\boldsymbol{x}_2 d\boldsymbol{x}_3 d\boldsymbol{p}_1 d\boldsymbol{p}_2 d\boldsymbol{p}_3 f^{(n)}_{h_1h_2h_3}(\boldsymbol{x}_1,\boldsymbol{x}_2,\boldsymbol{x}_3;\boldsymbol{p}_1,\boldsymbol{p}_2,\boldsymbol{p}_3)\mathcal{R}_{H_j}(\boldsymbol{x}_1,\boldsymbol{x}_2,\boldsymbol{x}_3;\boldsymbol{p}_1,\boldsymbol{p}_2,\boldsymbol{p}_3,\boldsymbol{p}). \quad (16)$$

$N_{h_1h_2h_3}$ is the number of all possible $h_1h_2h_3$-clusters and it equals to $N_{h_1}N_{h_2}N_{h_3}$, $N_{h_1}(N_{h_1}-1)N_{h_3}$ for $h_1 \neq h_2 \neq h_3$, $h_1 = h_2 \neq h_3$, respectively. $f^{(n)}_{h_1h_2h_3}(\boldsymbol{x}_1,\boldsymbol{x}_2,\boldsymbol{x}_3;\boldsymbol{p}_1,\boldsymbol{p}_2,\boldsymbol{p}_3)$ is the normalized three-baryon joint coordinate-momentum distribution, and $\mathcal{R}_{H_j}(\boldsymbol{x}_1,\boldsymbol{x}_2,\boldsymbol{x}_3;\boldsymbol{p}_1,\boldsymbol{p}_2,\boldsymbol{p}_3,\boldsymbol{p})$ is the kernel function.

We rewrite the kernel function as

$$\mathcal{R}_{H_j}(\boldsymbol{x}_1,\boldsymbol{x}_2,\boldsymbol{x}_3;\boldsymbol{p}_1,\boldsymbol{p}_2,\boldsymbol{p}_3,\boldsymbol{p}) = g_{H_j}\mathcal{R}^{(x,p)}_{H_j}(\boldsymbol{x}_1,\boldsymbol{x}_2,\boldsymbol{x}_3;\boldsymbol{p}_1,\boldsymbol{p}_2,\boldsymbol{p}_3)\delta(\sum_{i=1}^{3}\boldsymbol{p}_i - \boldsymbol{p}). \quad (17)$$

The spin degeneracy factor $g_{H_j} = (2J_{H_j}+1)/[\prod\limits_{i=1}^{3}(2J_{h_i}+1)]$. The Dirac δ function guarantees the momentum conservation. $\mathcal{R}^{(x,p)}_{H_j}(\boldsymbol{x}_1,\boldsymbol{x}_2,\boldsymbol{x}_3;\boldsymbol{p}_1,\boldsymbol{p}_2,\boldsymbol{p}_3)$ solving from the Wigner transformation [69–71] is

$$\mathcal{R}^{(x,p)}_{H_j}(\boldsymbol{x}_1,\boldsymbol{x}_2,\boldsymbol{x}_3;\boldsymbol{p}_1,\boldsymbol{p}_2,\boldsymbol{p}_3) = 8^2 e^{-\frac{(\boldsymbol{x}'_1-\boldsymbol{x}'_2)^2}{2\sigma_1^2}} e^{-\frac{2(\frac{m_1\boldsymbol{x}'_1}{m_1+m_2}+\frac{m_2\boldsymbol{x}'_2}{m_1+m_2}-\boldsymbol{x}'_3)^2}{3\sigma_2^2}} e^{-\frac{2\sigma_1^2(m_2\boldsymbol{p}'_1-m_1\boldsymbol{p}'_2)^2}{(m_1+m_2)^2}} e^{-\frac{3\sigma_2^2[m_3\boldsymbol{p}'_1+m_3\boldsymbol{p}'_2-(m_1+m_2)\boldsymbol{p}'_3]^2}{2(m_1+m_2+m_3)^2}}. \quad (18)$$

The superscript '$'$' denotes the baryon coordinate or momentum in the rest frame of the $h_1h_2h_3$-cluster. The width parameter $\sigma_1 = \sqrt{\frac{m_3(m_1+m_2)(m_1+m_2+m_3)}{m_1m_2(m_1+m_2)+m_2m_3(m_2+m_3)+m_3m_1(m_3+m_1)}}R_{H_j}$, and $\sigma_2 = \sqrt{\frac{4m_1m_2(m_1+m_2+m_3)^2}{3(m_1+m_2)[m_1m_2(m_1+m_2)+m_2m_3(m_2+m_3)+m_3m_1(m_3+m_1)]}}R_{H_j}$, where R_{H_j} is the root-mean-square radius of the H_j.

Substituting Eqs. (17) and (18) into Eq. (16), we have

$$\begin{aligned} f_{H_j}(\boldsymbol{p}) = {} & 8^2 N_{h_1h_2h_3} g_{H_j} \int d\boldsymbol{x}_1 d\boldsymbol{x}_2 d\boldsymbol{x}_3 d\boldsymbol{p}_1 d\boldsymbol{p}_2 d\boldsymbol{p}_3 e^{-\frac{(\boldsymbol{x}'_1-\boldsymbol{x}'_2)^2}{2\sigma_1^2}} e^{-\frac{2(\frac{m_1\boldsymbol{x}'_1}{m_1+m_2}+\frac{m_2\boldsymbol{x}'_2}{m_1+m_2}-\boldsymbol{x}'_3)^2}{3\sigma_2^2}} f^{(n)}_{h_1h_2h_3}(\boldsymbol{x}_1,\boldsymbol{x}_2,\boldsymbol{x}_3;\boldsymbol{p}_1,\boldsymbol{p}_2,\boldsymbol{p}_3) \\ & \times e^{-\frac{2\sigma_1^2(m_2\boldsymbol{p}'_1-m_1\boldsymbol{p}'_2)^2}{(m_1+m_2)^2}} e^{-\frac{3\sigma_2^2[m_3\boldsymbol{p}'_1+m_3\boldsymbol{p}'_2-(m_1+m_2)\boldsymbol{p}'_3]^2}{2(m_1+m_2+m_3)^2}} \delta(\sum_{i=1}^{3}\boldsymbol{p}_i - \boldsymbol{p}). \end{aligned} \quad (19)$$

Approximating the gaussian form of the momentum-dependent kernel function to be δ function form and integrating $\boldsymbol{p}_1$, $\boldsymbol{p}_2$ and $\boldsymbol{p}_3$ from Eq. (19), we can obtain

$$\begin{aligned} f_{H_j}(\boldsymbol{p}) = {} & 8^2 N_{h_1h_2h_3} g_{H_j} \int d\boldsymbol{x}_1 d\boldsymbol{x}_2 d\boldsymbol{x}_3 d\boldsymbol{p}_1 d\boldsymbol{p}_2 d\boldsymbol{p}_3 f^{(n)}_{h_1h_2h_3}(\boldsymbol{x}_1,\boldsymbol{x}_2,\boldsymbol{x}_3;\boldsymbol{p}_1,\boldsymbol{p}_2,\boldsymbol{p}_3) e^{-\frac{(\boldsymbol{x}'_1-\boldsymbol{x}'_2)^2}{2\sigma_1^2}} e^{-\frac{2(\frac{m_1\boldsymbol{x}'_1}{m_1+m_2}+\frac{m_2\boldsymbol{x}'_2}{m_1+m_2}-\boldsymbol{x}'_3)^2}{3\sigma_2^2}} \\ & \times (\frac{\sqrt{\pi}}{\sqrt{2}\sigma_1})^3 (1+\frac{m_1}{m_2})^3 \delta(\boldsymbol{p}'_1 - \frac{m_1}{m_2}\boldsymbol{p}'_2)(\frac{\sqrt{2\pi}}{\sqrt{3}\sigma_2})^3(1+\frac{m_1}{m_3}+\frac{m_2}{m_3})^3\delta(\boldsymbol{p}'_1+\boldsymbol{p}'_2-\frac{m_1+m_2}{m_3}\boldsymbol{p}'_3)\delta(\sum_{i=1}^{3}\boldsymbol{p}_i - \boldsymbol{p}) \\ = {} & 8^2 N_{h_1h_2h_3} g_{H_j} \int d\boldsymbol{x}_1 d\boldsymbol{x}_2 d\boldsymbol{x}_3 d\boldsymbol{p}_1 d\boldsymbol{p}_2 d\boldsymbol{p}_3 f^{(n)}_{h_1h_2h_3}(\boldsymbol{x}_1,\boldsymbol{x}_2,\boldsymbol{x}_3;\boldsymbol{p}_1,\boldsymbol{p}_2,\boldsymbol{p}_3) e^{-\frac{(\boldsymbol{x}'_1-\boldsymbol{x}'_2)^2}{2\sigma_1^2}} e^{-\frac{2(\frac{m_1\boldsymbol{x}'_1}{m_1+m_2}+\frac{m_2\boldsymbol{x}'_2}{m_1+m_2}-\boldsymbol{x}'_3)^2}{3\sigma_2^2}} \\ & \times (\frac{\sqrt{\pi}}{\sqrt{2}\sigma_1})^3 (1+\frac{m_1}{m_2})^3 \gamma\delta(\boldsymbol{p}_1 - \frac{m_1}{m_2}\boldsymbol{p}_2)(\frac{\sqrt{2\pi}}{\sqrt{3}\sigma_2})^3(1+\frac{m_1}{m_3}+\frac{m_2}{m_3})^3\gamma\delta(\boldsymbol{p}_1+\boldsymbol{p}_2-\frac{m_1+m_2}{m_3}\boldsymbol{p}_3)\delta(\sum_{i=1}^{3}\boldsymbol{p}_i - \boldsymbol{p}) \\ = {} & 8^2 N_{h_1h_2h_3} g_{H_j} \gamma^2 (\frac{\pi}{\sqrt{3}\sigma_1\sigma_2})^3 \int d\boldsymbol{x}_1 d\boldsymbol{x}_2 d\boldsymbol{x}_3 f^{(n)}_{h_1h_2h_3}(\boldsymbol{x}_1,\boldsymbol{x}_2,\boldsymbol{x}_3;\frac{m_1\boldsymbol{p}}{m_1+m_2+m_3},\frac{m_2\boldsymbol{p}}{m_1+m_2+m_3},\frac{m_3\boldsymbol{p}}{m_1+m_2+m_3}) \\ & \times e^{-\frac{(\boldsymbol{x}'_1-\boldsymbol{x}'_2)^2}{2\sigma_1^2}} e^{-\frac{2(\frac{m_1\boldsymbol{x}'_1}{m_1+m_2}+\frac{m_2\boldsymbol{x}'_2}{m_1+m_2}-\boldsymbol{x}'_3)^2}{3\sigma_2^2}}. \end{aligned} \quad (20)$$

Changing coordinate variables in Eq. (20) to be $\boldsymbol{Y} = (m_1\boldsymbol{x}_1 + m_2\boldsymbol{x}_2 + m_3\boldsymbol{x}_3)/(m_1+m_2+m_3)$, $\boldsymbol{r}_1 = (\boldsymbol{x}_1 - \boldsymbol{x}_2)/\sqrt{2}$ and $\boldsymbol{r}_2 = \sqrt{\frac{2}{3}}(\frac{m_1\boldsymbol{x}_1}{m_1+m_2}+\frac{m_2\boldsymbol{x}_2}{m_1+m_2}-\boldsymbol{x}_3)$ as in Refs. [69–71], we have

$$f_{H_j}(\boldsymbol{p}) = 8^2 N_{h_1h_2h_3} g_{H_j} \gamma^2 (\frac{\pi}{\sqrt{3}\sigma_1\sigma_2})^3$$

$$\times \int 3^{3/2} d\boldsymbol{Y} d\boldsymbol{r_1} d\boldsymbol{r_2} f^{(n)}_{h_1h_2h_3}(\boldsymbol{Y},\boldsymbol{r}_1,\boldsymbol{r}_2;\frac{m_1\boldsymbol{p}}{m_1+m_2+m_3},\frac{m_2\boldsymbol{p}}{m_1+m_2+m_3},\frac{m_3\boldsymbol{p}}{m_1+m_2+m_3})e^{-\frac{r_1'^2}{\sigma_1^2}}e^{-\frac{r_2'^2}{\sigma_2^2}}. \quad (21)$$

We also assume the center of mass coordinate in joint distribution is factorized, i.e.,

$$3^{3/2} f^{(n)}_{h_1h_2h_3}(\boldsymbol{Y},\boldsymbol{r}_1,\boldsymbol{r}_2;\frac{m_1\boldsymbol{p}}{m_1+m_2+m_3},\frac{m_2\boldsymbol{p}}{m_1+m_2+m_3},\frac{m_3\boldsymbol{p}}{m_1+m_2+m_3})$$
$$= f^{(n)}_{h_1h_2h_3}(\boldsymbol{Y}) f^{(n)}_{h_1h_2h_3}(\boldsymbol{r}_1,\boldsymbol{r}_2;\frac{m_1\boldsymbol{p}}{m_1+m_2+m_3},\frac{m_2\boldsymbol{p}}{m_1+m_2+m_3},\frac{m_3\boldsymbol{p}}{m_1+m_2+m_3}). \quad (22)$$

Substituting Eq. (22) into Eq. (21), we have

$$f_{H_j}(\boldsymbol{p}) = 8^2 N_{h_1h_2h_3} g_{H_j} \gamma^2 (\frac{\pi}{\sqrt{3}\sigma_1\sigma_2})^3 \int d\boldsymbol{r_1} d\boldsymbol{r_2} f^{(n)}_{h_1h_2h_3}(\boldsymbol{r}_1,\boldsymbol{r}_2;\frac{m_1\boldsymbol{p}}{m_1+m_2+m_3},\frac{m_2\boldsymbol{p}}{m_1+m_2+m_3},\frac{m_3\boldsymbol{p}}{m_1+m_2+m_3})$$
$$\times e^{-\frac{r_1'^2}{\sigma_1^2}} e^{-\frac{r_2'^2}{\sigma_2^2}}. \quad (23)$$

Adopting gaussian forms for the relative coordinate distributions [66, 72–74], we have

$$f^{(n)}_{h_1h_2h_3}(\boldsymbol{r}_1,\boldsymbol{r}_2;\frac{m_1\boldsymbol{p}}{m_1+m_2+m_3},\frac{m_2\boldsymbol{p}}{m_1+m_2+m_3},\frac{m_3\boldsymbol{p}}{m_1+m_2+m_3})$$
$$= \frac{1}{[\pi C_1 R_f^2(\boldsymbol{p})]^{3/2}} e^{-\frac{r_1^2}{C_1 R_f^2(\boldsymbol{p})}} \frac{1}{[\pi C_2 R_f^2(\boldsymbol{p})]^{3/2}} e^{-\frac{r_2^2}{C_2 R_f^2(\boldsymbol{p})}} f^{(n)}_{h_1h_2h_3}(\frac{m_1\boldsymbol{p}}{m_1+m_2+m_3},\frac{m_2\boldsymbol{p}}{m_1+m_2+m_3},\frac{m_3\boldsymbol{p}}{m_1+m_2+m_3}). \quad (24)$$

Comparing relations of $\boldsymbol{r}_1$, $\boldsymbol{r}_2$ with $\boldsymbol{x}_1$, $\boldsymbol{x}_2$, $\boldsymbol{x}_3$ to that of $\boldsymbol{r}$ with $\boldsymbol{x}_1$, $\boldsymbol{x}_2$ in Sec. II A, we see that C_1 is equal to C_0 and C_2 is $4C_0/3$ [66, 72–74]. Substituting Eq. (24) into Eq. (23) and considering the coordinate Lorentz transformation, we integrate from the relative coordinate variables and obtain

$$f_{H_j}(\boldsymbol{p}) = \frac{8^2\pi^3 g_{H_j}\gamma^2}{3^{3/2}\left[C_1R_f^2(\boldsymbol{p})+\sigma_1^2\right]\sqrt{C_1[R_f(\boldsymbol{p})/\gamma]^2+\sigma_1^2}\left[C_2R_f^2(\boldsymbol{p})+\sigma_2^2\right]\sqrt{C_2[R_f(\boldsymbol{p})/\gamma]^2+\sigma_2^2}}$$
$$\times f_{h_1h_2h_3}(\frac{m_1\boldsymbol{p}}{m_1+m_2+m_3},\frac{m_2\boldsymbol{p}}{m_1+m_2+m_3},\frac{m_3\boldsymbol{p}}{m_1+m_2+m_3}). \quad (25)$$

Ignoring correlations between h_1, h_2 and h_3, we have the three-dimensional momentum distribution of H_j as

$$f_{H_j}(\boldsymbol{p}) = \frac{8^2\pi^3 g_{H_j}\gamma^2}{3^{3/2}\left[C_1R_f^2(\boldsymbol{p})+\sigma_1^2\right]\sqrt{C_1[R_f(\boldsymbol{p})/\gamma]^2+\sigma_1^2}\left[C_2R_f^2(\boldsymbol{p})+\sigma_2^2\right]\sqrt{C_2[R_f(\boldsymbol{p})/\gamma]^2+\sigma_2^2}}$$
$$\times f_{h_1}(\frac{m_1\boldsymbol{p}}{m_1+m_2+m_3}) f_{h_2}(\frac{m_2\boldsymbol{p}}{m_1+m_2+m_3}) f_{h_3}(\frac{m_3\boldsymbol{p}}{m_1+m_2+m_3}). \quad (26)$$

Finally, we have the Lorentz invariant momentum distribution as

$$f^{(inv)}_{H_j}(p_T,y) = \frac{8^2\pi^3 g_{H_j}}{3^{3/2}\left[C_1R_f^2(p_T,y)+\sigma_1^2\right]\sqrt{C_1[R_f(p_T,y)/\gamma]^2+\sigma_1^2}\left[C_2R_f^2(p_T,y)+\sigma_2^2\right]\sqrt{C_2[R_f(p_T,y)/\gamma]^2+\sigma_2^2}}$$
$$\times \frac{m_{H_j}}{m_1m_2m_3} f^{(inv)}_{h_1}(\frac{m_1p_T}{m_1+m_2+m_3},y) f^{(inv)}_{h_2}(\frac{m_2p_T}{m_1+m_2+m_3},y) f^{(inv)}_{h_3}(\frac{m_3p_T}{m_1+m_2+m_3},y). \quad (27)$$

As a short summary of this section, we want to state that Eqs. (15) and (27) give: (i) the relationships of dibaryon states and tribaryon states with primordial baryons in momentum space in the laboratory frame, (ii) effects of different factors on dibaryon or tribaryon production such as the whole hadronic system scale and the size of the formed composite object. They can be directly used to calculate the productions of light nuclei, hypernuclei, and even other hadronic molecular states. And what's more, they can be conveniently used to investigate production correlations of different species of composite objects. Formulae for the antiparticles are the same as these dibaryon and tribaryon states, and we leave out the duplication. Their applications at midrapidity (i.e., $y = 0$) in heavy ion collisions at the LHC will be shown in the following sections.

III. RESULTS OF LIGHT NUCLEI

In this section, we use the coalescence model to study productions of d, $^3\overline{\text{He}}$ and $\bar{t}$ at midrapidity in Pb+Pb collisions at $\sqrt{s_{NN}} = 5.02$ TeV. We first calculate the coalescence factors B_2, B_3 and discuss their centrality and p_T-dependent behaviors. We then compute the p_T spectra of d, $^3\overline{\text{He}}$ and $\bar{t}$. We finally calculate the averaged transverse momenta $\langle p_T \rangle$, the yield rapidity densities dN/dy and the yield ratios of different light nuclei.

A. The coalescence factor of light nuclei

The coalescence factor B_A is defined as

$$B_A(p_T) = \frac{f^{(inv)}_{d,^3\text{He},t}(p_T)}{\left[f^{(inv)}_p(\frac{p_T}{A})\right]^Z \left[f^{(inv)}_n(\frac{p_T}{A})\right]^{A-Z}}, \quad (28)$$

where A is the mass number and Z is the charge of the light nuclei. It is a unique link between the formed light nuclei and the primordial nucleons. Much effort has been put into B_A in different coalescence models [11, 13, 57–59, 75]. From Eqs. (15) and (27), we respectively have for d, ^{3}He and t

$$B_2(p_T) = \frac{m_d g_d(\sqrt{2\pi})^3}{m_p m_n \left[C_0 R_f^2(p_T) + \sigma_d^2\right] \sqrt{C_0[\frac{R_f(p_T)}{\gamma}]^2 + \sigma_d^2}}, \quad (29)$$

$$B_3(p_T) = \frac{64\pi^3 g_{^3\text{He}}}{3^{\frac{3}{2}} \left[C_1 R_f^2(p_T) + \sigma_{^3\text{He}}^2\right] \sqrt{C_1[\frac{R_f(p_T)}{\gamma}]^2 + \sigma_{^3\text{He}}^2}} \times \frac{m_{^3\text{He}}}{m_p^2 m_n \left[C_2 R_f^2(p_T) + \sigma_{^3\text{He}}^2\right] \sqrt{C_2[\frac{R_f(p_T)}{\gamma}]^2 + \sigma_{^3\text{He}}^2}}, \quad (30)$$

$$B_3(p_T) = \frac{64\pi^3 g_t}{3^{\frac{3}{2}} \left[C_1 R_f^2(p_T) + \sigma_t^2\right] \sqrt{C_1[\frac{R_f(p_T)}{\gamma}]^2 + \sigma_t^2}} \times \frac{m_t}{m_p m_n^2 \left[C_2 R_f^2(p_T) + \sigma_t^2\right] \sqrt{C_2[\frac{R_f(p_T)}{\gamma}]^2 + \sigma_t^2}}. \quad (31)$$

Here $\sigma_d = \sqrt{\frac{4}{3}} R_d$, and the root-mean-square radius of the deuteron $R_d = 2.1421$ fm [76]. $\sigma_{^3\text{He}} = R_{^3\text{He}} = 1.9661$ fm and $\sigma_t = R_t = 1.7591$ fm [76]. $m_{p,n}$ denotes the nucleon mass and $m_{d,^3\text{He},t}$ the mass of the d, ^{3}He or t.

To further compute B_2 and B_3, the specific form of $R_f(p_T)$ is necessary. Similar to Ref. [67], the dependence of $R_f(p_T)$ on centrality and p_T is considered to factorize into a linear dependence on the cube root of the pseudorapidity density of charged particles $(dN_{ch}/d\eta)^{1/3}$ and a power-law dependence on the transverse mass of the formed light nucleus [74]. So we have

$$R_f(p_T) = a \times (dN_{ch}/d\eta)^{\frac{1}{3}} \times \left(\sqrt{p_T^2 + m^2_{d,^3\text{He},t}}\right)^b, \quad (32)$$

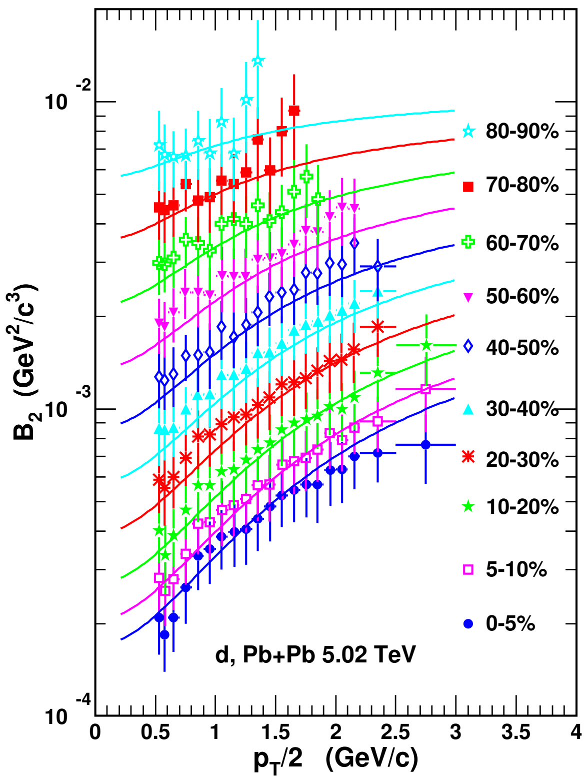

Fig. 1. The B_2 of d as a function of $p_T/2$ in different centralities in Pb+Pb collisions at $\sqrt{s_{NN}} = 5.02$ TeV. Symbols with error bars are experimental data [77] and solid lines are theoretical results.

where a and b are free parameters. Their values in Pb+Pb collisions at $\sqrt{s_{NN}} = 5.02$ TeV are (0.70,-0.31) for d and (0.66,-0.31) for ^{3}He and t, which are determined by reproducing the data of p_T spectra of d and ^{3}He in the most central 0-5% centrality. Here b is set to be centrality independent, which is consistent with that in hydrodynamics [78] and that in STAR measurements of two-pion interferometry in central and semi-central Au+Au collisions [79]. a is also set to be centrality-independent, the same as that in our previous work [67].

We use the data of $dN_{ch}/d\eta$ in Ref. [80] to evaluate $R_f(p_T)$, and then compute coalescence factors B_2 and B_3. Fig. 1 shows B_2 of d as a function of the transverse momentum scaled by the mass number $p_T/2$ in different centralities in Pb+Pb collisions at $\sqrt{s_{NN}} = 5.02$ TeV. Symbols with error bars are experimental data [77] and solid lines are theoretical results of the coalescence model. From Fig. 1, one can see from central to peripheral collisions B_2 exhibits an increasing trend, which is due to the decreasing scale of the created hadronic system. For a certain centrality, B_2 increases as a function of $p_T/2$. This increased behavior results on one hand from the Lorentz contraction factor γ, which has been studied in Ref. [66]. On the other hand, it results from the decreasing R_f with increasing p_T. The rising behavior of the experimental data as a function of $p_T/2$ from central to peripheral collisions can be quantitatively described by the coalescence model.

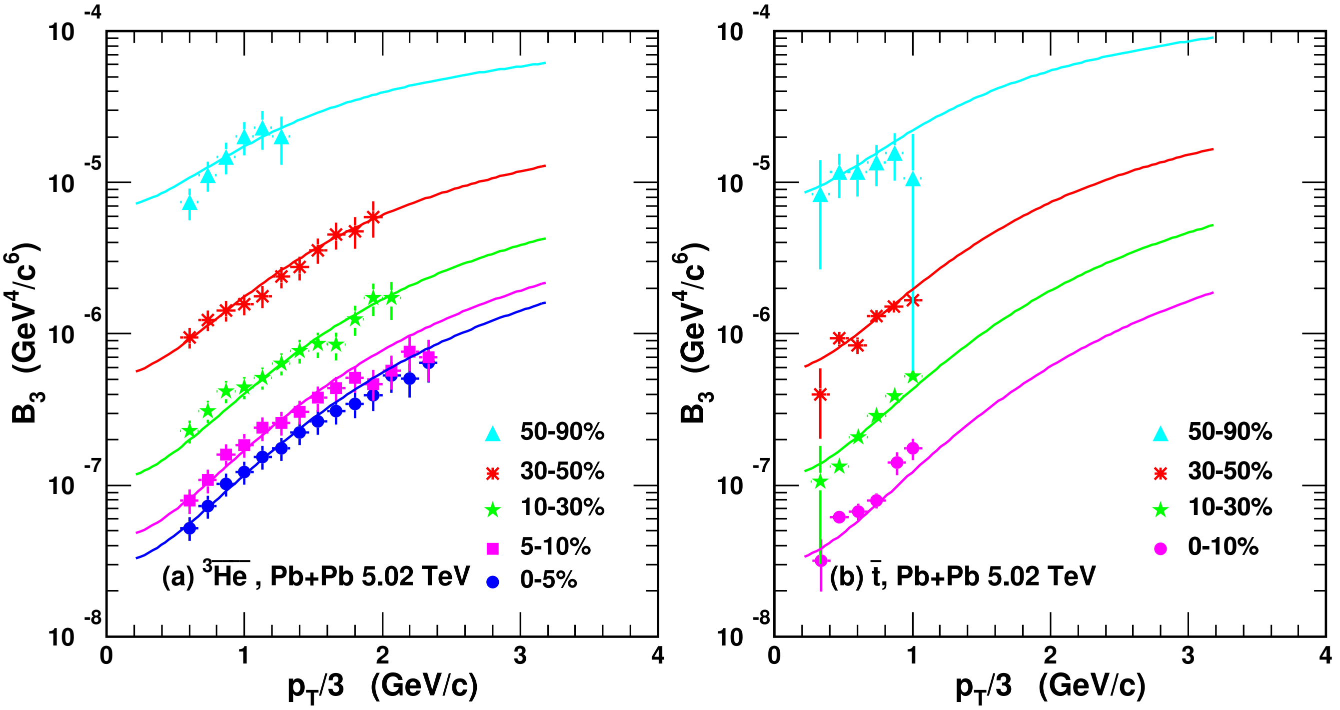

Fig. 2. The B_3 of (a) $^3\overline{\mathrm{He}}$ and (b) $\bar{t}$ as a function of $p_T/3$ in different centralities in Pb+Pb collisions at $\sqrt{s_{NN}} = 5.02$ TeV. Symbols with error bars are experimental data [30] and solid lines are theoretical results.

Fig. 2 shows B_3 of $^3\overline{\mathrm{He}}$ and that of $\bar{t}$ as a function of $p_T/3$ in different centralities in Pb+Pb collisions at $\sqrt{s_{NN}} = 5.02$ TeV. Symbols with error bars are experimental data [30] and solid lines are theoretical results. Similarly, as B_2, experimental data of B_3 also exhibit a rising trend as a function of $p_T/3$, which is reproduced well by the coalescence model from central to peripheral collisions. Fig. 1 and Fig. 2 show that the centrality and p_T-dependent behaviors of B_2 and B_3 are simultaneously explained by the coalescence model. Our extracted results for $R_f(p_T)$ can provide quantitative references for future measurements of HBT interferometry radius from two-nucleon correlations. Through light nucleus production, we provide an alternative way to the HBT interferometry radius of the hadronic source system.

B. The p_T spectra of light nuclei

The p_T spectra of primordial nucleons are necessary inputs for computing p_T distributions of light nuclei in the coalescence model. We here use the blast-wave model to get p_T distribution functions of primordial protons by fitting the experimental data of prompt (anti)protons in Ref. [80]. The blast-wave function [81] is given as

$$\frac{d^2N}{2\pi p_T dp_T dy} \propto \int_0^R r dr m_T I_0\left(\frac{p_T sinh\rho}{T_{kin}}\right) K_1\left(\frac{m_T cosh\rho}{T_{kin}}\right), \quad (33)$$

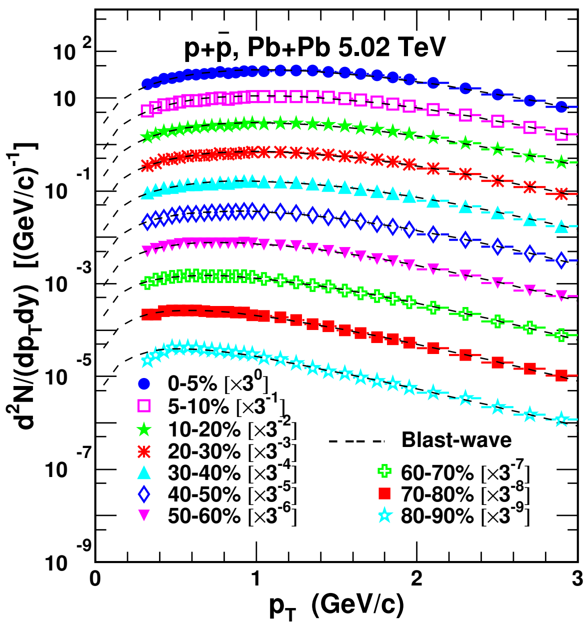

Fig. 3. The p_T spectra of prompt protons plus antiprotons in different centralities in Pb+Pb collisions at $\sqrt{s_{NN}} = 5.02$ TeV. Symbols with error bars are experimental data [80] and dashed lines are results of the blast-wave model.

where r is the radial distance in the transverse plane and R is the fireball radius. I_0 and K_1 are the modified Bessel functions, and the velocity profile $\rho = tanh^{-1}\beta_T =$

$tanh^{-1}[\beta_s(\frac{r}{R})^n]$. The kinetic freeze-out temperature T_{kin}, the averaged radial expansion velocity $\langle\beta_T\rangle$ and n are fit parameters. Their values can be found in Ref. [80].

Fig. 3 shows the p_T spectra of prompt protons plus antiprotons in different centralities in Pb+Pb collisions at $\sqrt{s_{NN}} = 5.02$ TeV. Symbols with error bars are experimental data [80], and dashed lines are the results of the blast-wave model. The p_T spectra in different centralities are scaled by different factors for clarity as shown in the figure. For the primordial neutron p_T spectra, we adopt the same as those of primordial protons as we focus on light nucleus production at midrapidity at so high LHC energy that the isospin symmetry is well satisfied.

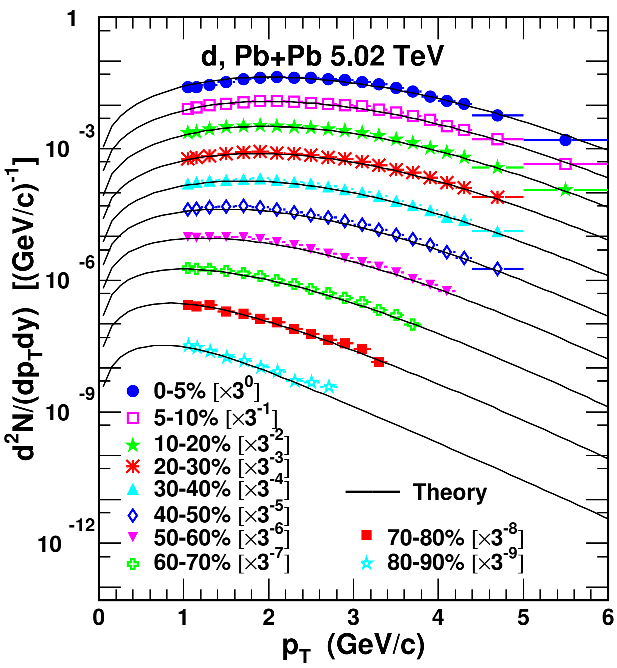

Fig. 4. The p_T spectra of deuterons in different centralities in Pb+Pb collisions at $\sqrt{s_{NN}} = 5.02$ TeV. Symbols with error bars are experimental data [77] and solid lines are theoretical results.

We first calculate the p_T spectra of deuterons in Pb+Pb collisions at $\sqrt{s_{NN}} = 5.02$ TeV in $0-5\%$, $5-10\%$, $10-20\%$, $20-30\%$, $30-40\%$, $40-50\%$, $50-60\%$, $60-70\%$, $70-80\%$ and $80-90\%$ centralities. Different solid lines scaled by different factors for clarity in Fig. 4 are our theoretical results. Symbols with error bars are experimental data from the ALICE collaboration [30]. We then compute the p_T spectra of $^3\overline{\text{He}}$ and $\bar{t}$ in Pb+Pb collisions at $\sqrt{s_{NN}} = 5.02$ TeV in different centralities. Different solid lines in Fig. 5 are our theoretical results, which agree with the available data denoted by filled symbols [30]. From Fig. 4 and Fig. 5, one can see the nucleon coalescence is the dominant mechanism for light nucleus production in Pb+Pb collisions at $\sqrt{s_{NN}} = 5.02$ TeV. More precise measurements for $^3\overline{\text{He}}$ and $\bar{t}$ in wide p_T range in the forthcoming future can help further test the coalescence mechanism, especially in peripheral Pb+Pb collisions.

C. Averaged transverse momenta and yield rapidity densities of light nuclei

We here study the averaged transverse momenta $\langle p_T\rangle$ and yield rapidity densities dN/dy of d, $^3\overline{\text{He}}$ and $\bar{t}$. Our theoretical results are in the fourth and sixth columns in Table 1. Experimental data in the third and fifth columns are from Refs. [30, 77]. A decreasing trend for both $\langle p_T\rangle$ and dN/dy from central to peripheral collisions is observed. This is because in more central collisions more energy is deposited in the midrapidity region and collective evolution exists longer. Theoretical results for d, $^3\overline{\text{He}}$ and $\bar{t}$ are consistent with the corresponding data within the experimental uncertainties except for a very little underestimation for the dN/dy of $\bar{t}$ in a peripheral 50-90% collision. Such underestimation needs to be confirmed by future precise data.

D. Yield ratios of light nuclei

Yield ratios carry information on intrinsic production correlations of different light nuclei and are predicted to have nontrivial behaviors [67]. In this subsection, we study the centrality dependence of different yield ratios, such as d/p, $^3\overline{\text{He}}/\bar{p}$, d/p^2, $^3\overline{\text{He}}/\bar{p}^3$ and $\bar{t}/^3\overline{\text{He}}$.

Fig. 6 (a) and (b) show the $dN_{ch}/d\eta$ dependence of d/p and $^3\overline{\text{He}}/\bar{p}$ in Pb+Pb collisions at $\sqrt{s_{NN}} = 5.02$ TeV. Filled circles with error bars are experimental data [82], and open circles connected with dashed lines to guide the eye are theoretical results. From Eq. (15) we approximately have the p_T-integrated yield ratio

$$\frac{d}{p} \propto \frac{N_p}{\langle R_f\rangle^3\left(C_0+\frac{\sigma_d^2}{\langle R_f\rangle^2}\right)\sqrt{\frac{C_0}{\langle\gamma\rangle^2}+\frac{\sigma_d^2}{\langle R_f\rangle^2}}}$$

$$=\frac{N_p}{\langle R_f\rangle^3/\langle\gamma\rangle}\times\frac{1}{\left(C_0+\frac{\sigma_d^2}{\langle R_f\rangle^2}\right)\sqrt{C_0+\frac{\sigma_d^2}{\langle R_f\rangle^2/\langle\gamma\rangle^2}}}, \quad (34)$$

where angle brackets denote the averaged values. Eq. (34) gives that the behavior of d/p is determined by two factors. One is the nucleon number density $\frac{N_p}{\langle R_f\rangle^3/\langle\gamma\rangle}$ and the other is the suppression effect from the relative size of the d to the hadronic source system $\frac{\sigma_d}{\langle R_f\rangle}$. Similar case holds for $^3\overline{\text{He}}/\bar{p}$. The nucleon number density decreases especially from semi-central to central collisions [80], which makes d/p and $^3\overline{\text{He}}/\bar{p}$ decrease with the increasing $dN_{ch}/d\eta$. The relative size $\frac{\sigma_d}{\langle R_f\rangle}$ decreases and its suppression effect becomes weak in large hadronic systems, which makes d/p and $^3\overline{\text{He}}/\bar{p}$ increase with the increasing $dN_{ch}/d\eta$ [83]. For very high $dN_{ch}/d\eta$ area, the difference of the suppression extents in different centralities becomes insignificant and the decreasing nucleon number density dominates the decreasing behavior of d/p and $^3\overline{\text{He}}/\bar{p}$. For low $dN_{ch}/d\eta$ area, different suppression extents of the relative size in different centralities make d/p and $^3\overline{\text{He}}/\bar{p}$ increase as a function of $dN_{ch}/d\eta$. The final conjunct result from the nucleon number density and the suppression effect

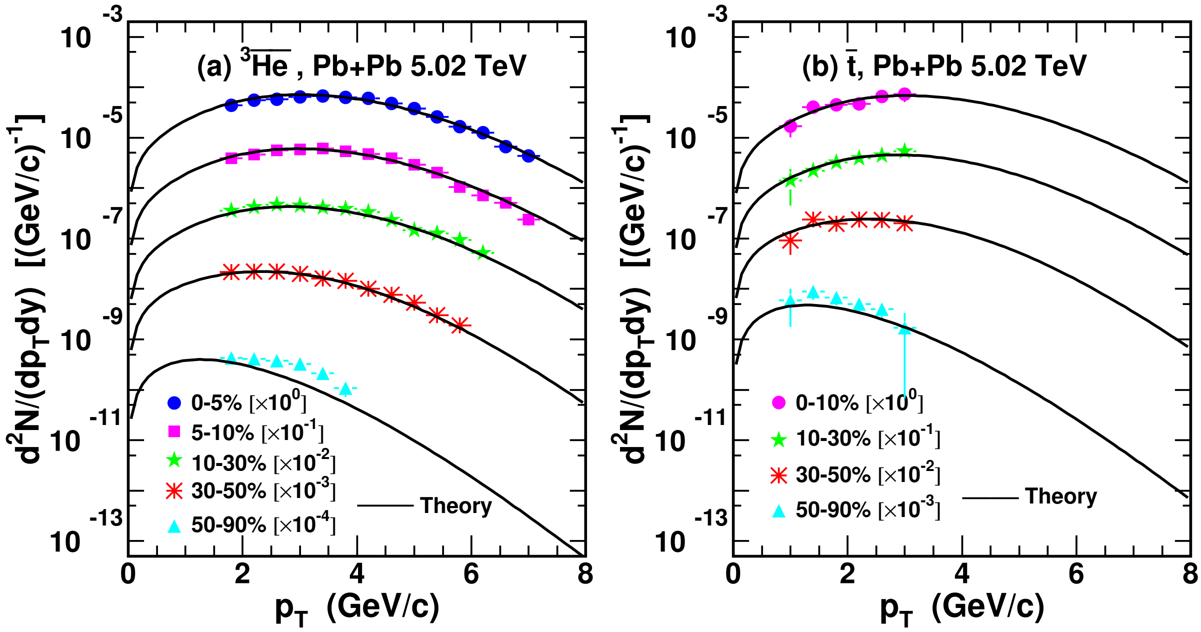

Fig. 5. The p_T spectra of (a) $^{3}\overline{\mathrm{He}}$ and (b) $\bar{t}$ in different centralities in Pb+Pb collisions at $\sqrt{s_{NN}} = 5.02$ TeV. Filled symbols with error bars are experimental data [30] and solid lines are theoretical results.

Table 1. Averaged transverse momenta $\langle p_T \rangle$ and yield rapidity densities dN/dy of d, $^{3}\overline{\mathrm{He}}$ and $\bar{t}$ in different centralities in Pb+Pb collisions at $\sqrt{s_{NN}} = 5.02$ TeV. Experimental data in the third and fifth columns are from Refs. [30, 77]. Theoretical results are in the fourth and sixth columns.

	Centrality	$\langle p_T \rangle$ (GeV/c) Data	Theory	dN/dy Data	Theory
d	$0-5\%$	$2.45 \pm 0.00 \pm 0.09$	2.37	$(1.19 \pm 0.00 \pm 0.21) \times 10^{-1}$	1.22×10^{-1}
	$5-10\%$	$2.41 \pm 0.01 \pm 0.10$	2.33	$(1.04 \pm 0.00 \pm 0.19) \times 10^{-1}$	1.01×10^{-1}
	$10-20\%$	$2.34 \pm 0.00 \pm 0.11$	2.28	$(8.42 \pm 0.02 \pm 1.50) \times 10^{-2}$	7.86×10^{-2}
	$20-30\%$	$2.21 \pm 0.00 \pm 0.12$	2.18	$(6.16 \pm 0.02 \pm 1.10) \times 10^{-2}$	5.58×10^{-2}
	$30-40\%$	$2.05 \pm 0.00 \pm 0.12$	2.04	$(4.25 \pm 0.01 \pm 0.75) \times 10^{-2}$	3.82×10^{-2}
	$40-50\%$	$1.88 \pm 0.01 \pm 0.12$	1.87	$(2.73 \pm 0.01 \pm 0.48) \times 10^{-2}$	2.46×10^{-2}
	$50-60\%$	$1.70 \pm 0.01 \pm 0.11$	1.66	$(1.62 \pm 0.01 \pm 0.28) \times 10^{-2}$	1.47×10^{-2}
	$60-70\%$	$1.46 \pm 0.01 \pm 0.12$	1.45	$(8.35 \pm 0.14 \pm 1.43) \times 10^{-3}$	7.58×10^{-3}
	$70-80\%$	$1.27 \pm 0.02 \pm 0.11$	1.25	$(3.52 \pm 0.06 \pm 0.63) \times 10^{-3}$	3.22×10^{-3}
	$80-90\%$	$1.09 \pm 0.02 \pm 0.40$	1.10	$(1.13 \pm 0.03 \pm 0.23) \times 10^{-3}$	0.925×10^{-3}
$^{3}\overline{\mathrm{He}}$	$0-5\%$	$3.465 \pm 0.013 \pm 0.154 \pm 0.144$	3.26	$(24.70 \pm 0.28 \pm 2.29 \pm 0.30) \times 10^{-5}$	25.6×10^{-5}
	$5-10\%$	$3.368 \pm 0.014 \pm 0.141 \pm 0.132$	3.21	$(20.87 \pm 0.26 \pm 1.95 \pm 0.43) \times 10^{-5}$	21.4×10^{-5}
	$10-30\%$	$3.237 \pm 0.021 \pm 0.157 \pm 0.150$	3.08	$(15.94 \pm 0.31 \pm 1.53 \pm 0.34) \times 10^{-5}$	14.8×10^{-5}
	$30-50\%$	$2.658 \pm 0.016 \pm 0.084 \pm 0.049$	2.64	$(7.56 \pm 0.13 \pm 0.70 \pm 0.10) \times 10^{-5}$	7.16×10^{-5}
	$50-90\%$	$2.057 \pm 0.023 \pm 0.090 \pm 0.027$	1.77	$(1.19 \pm 0.08 \pm 0.16 \pm 0.14) \times 10^{-5}$	0.931×10^{-5}
$\bar{t}$	$0-10\%$	$3.368 \pm 0.241 \pm 0.060$	3.27	$(24.45 \pm 1.75 \pm 2.71) \times 10^{-5}$	24.6×10^{-5}
	$10-30\%$	$3.015 \pm 0.286 \pm 0.040$	3.11	$(14.19 \pm 1.35 \pm 1.29) \times 10^{-5}$	15.9×10^{-5}
	$30-50\%$	$2.524 \pm 0.593 \pm 0.180$	2.68	$(7.24 \pm 1.70 \pm 0.65) \times 10^{-5}$	7.97×10^{-5}
	$50-90\%$	$1.636 \pm 0.226 \pm 0.040$	1.80	$(1.66 \pm 0.23 \pm 0.16) \times 10^{-5}$	1.14×10^{-5}

makes d/p and $^{3}\overline{\mathrm{He}}/\bar{p}$ first increase from peripheral to semi-central collisions and then decrease from semi-central to central collisions, just as shown in Fig. 6 (a) and (b).

Fig. 6 (c) and (d) show d/p^2 and $^{3}\overline{\mathrm{He}}/\bar{p}^3$ as a function of $dN_{ch}/d\eta$ in Pb+Pb collisions at $\sqrt{s_{NN}} = 5.02$ TeV. Filled circles with error bars are experimental data [82]. Open circles connected with dashed lines to guide the eye are theoretical results. Both of them give explicit decreasing trends with the increasing $dN_{ch}/d\eta$, which are very different from the previous d/p and $^{3}\overline{\mathrm{He}}/\bar{p}$. Recalling that d/p^2 and $^{3}\overline{\mathrm{He}}/\bar{p}^3$ represent the probability of any pn-pair coalescing into a deuteron and that of any $\bar{p}\bar{p}\bar{n}$-cluster coalescing into a $^{3}\overline{\mathrm{He}}$. This means that it is more difficult for any pn-pair or $\bar{p}\bar{p}\bar{n}$-cluster to recombine into a deuteron or $^{3}\overline{\mathrm{He}}$ in the larger

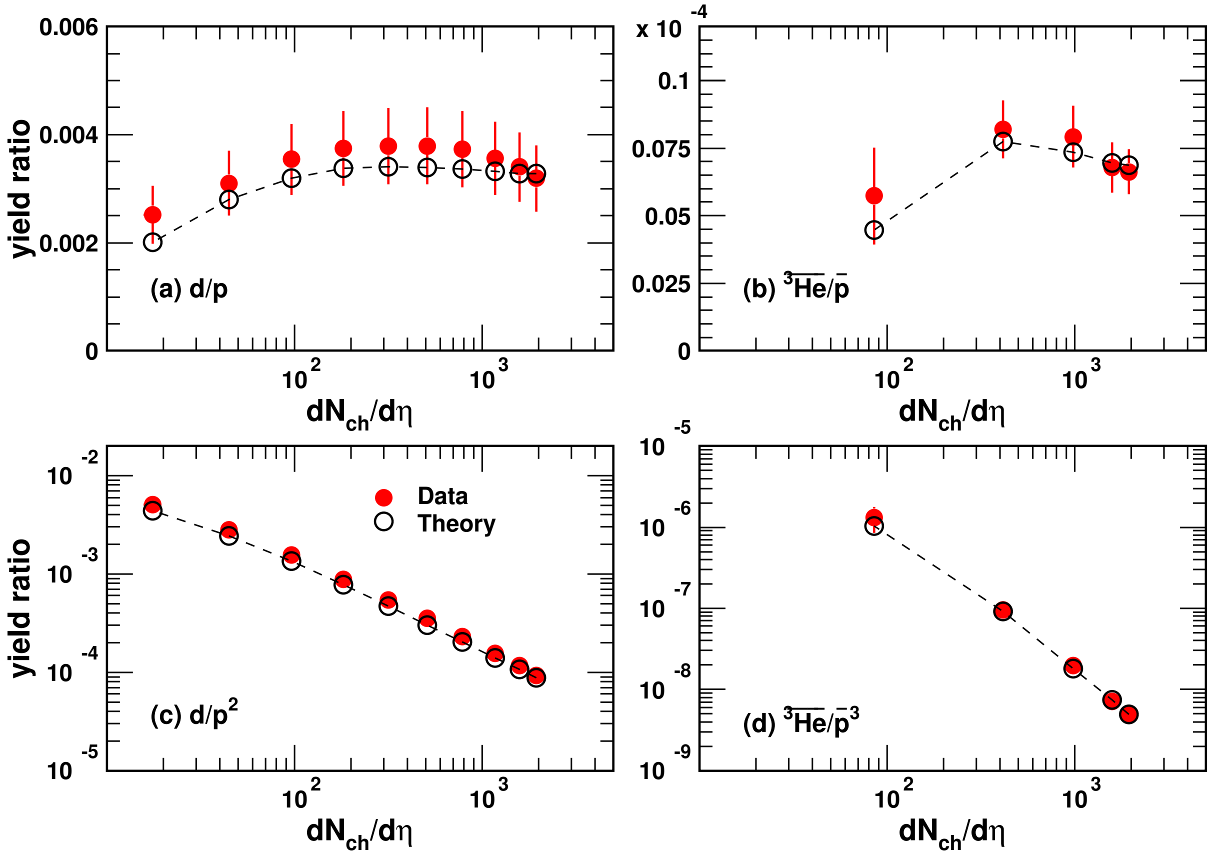

Fig. 6. Yield ratios (a) d/p, (b) $^3\overline{\mathrm{He}}/\bar{p}$, (c) d/p^2 and (d) $^3\overline{\mathrm{He}}/\bar{p}^3$ as a function of $dN_{ch}/d\eta$ in Pb+Pb collisions at $\sqrt{s_{NN}} = 5.02$ TeV. Filled circles with error bars are experimental data [30, 77] and open circles connected with dashed lines to guide the eye are theoretical results.

hadronic system produced in a more central collision.

The yield ratio $t/^3\mathrm{He}$ is proposed as a valuable probe to distinguish the thermal production and the coalescence production for light nuclei [67]. In the coalescence picture, it is always larger than one and approaches one at large R_f where the suppression effect from the nucleus size can be ignored. The smaller R_f, the higher deviation of $t/^3\mathrm{He}$ from one. The same case holds for $\bar{t}/^3\overline{\mathrm{He}}$. Fig. 7 shows $\bar{t}/^3\overline{\mathrm{He}}$ as a function of p_T in Pb+Pb collisions at $\sqrt{s_{NN}} = 5.02$ TeV in different centralities 0-10%, 10-30%, 30-50% and 50-90%. Filled circles with error bars are experimental data [30] and solid lines are theoretical results. The reference line of one is plotted with dotted lines. With the increasing p_T, R_f decreases, so our theoretical results increase. This feature is very different from that in the thermal model, where the expectation for this ratio is one [47]. The trend of the data in 0-10%, 10-30%, and 30-50% centralities indicates an increasing hint but a final conclusion is hard to make due to the limited p_T range and the large error bars. Data in the peripheral 50-90% centrality seem to decrease, but further more precise measurements are needed to confirm. More precise data in the near future can be used to further distinguish production mechanisms of $^3\overline{\mathrm{He}}$ and $\bar{t}$.

The p_T-integrated yield ratio $\bar{t}/^3\overline{\mathrm{He}}$ as a function of $dN_{ch}/d\eta$ is in Fig. 8. Filled circles with error bars are experimental data [30] and open circles connected with the dashed line to guide the eye are theoretical results. The reference line of one is also plotted with the dotted line. $\bar{t}/^3\overline{\mathrm{He}}$ exhibits a decreasing trend. This is because larger $dN_{ch}/d\eta$, i.e., larger R_f, makes $\bar{t}/^3\overline{\mathrm{He}}$ decrease closer to one. Theoretical results of $\bar{t}/^3\overline{\mathrm{He}}$ in the coalescence model give a non-flat behavior as a function of $dN_{ch}/d\eta$. This is due to different relative production suppression between $^3\overline{\mathrm{He}}$ and $\bar{t}$ from their own sizes at different hadronic system scales.

IV. RESULTS OF HYPERTRITON AND Ω-HYPERNUCLEI

In this section, we use the coalescence model in Sec. II to study productions of the hypertriton $^3_\Lambda\mathrm{H}$ and Ω-hypernuclei. We give results of the p_T spectra, the averaged p_T, and the yield rapidity densities of $^3_\Lambda\mathrm{H}$. We present predictions of different Ω-hypernuclei, $H(p\Omega^-)$, $H(n\Omega^-)$ and $H(pn\Omega^-)$. We propose two groups of observables, both of which exhibit novel behaviors. One group refers to the averaged transverse momentum ratios of light nuclei to the proton and hypernuclei to hyperons. The other is the centrality-dependent yield ratios of light (hyper-)nuclei to the proton (hyperons).

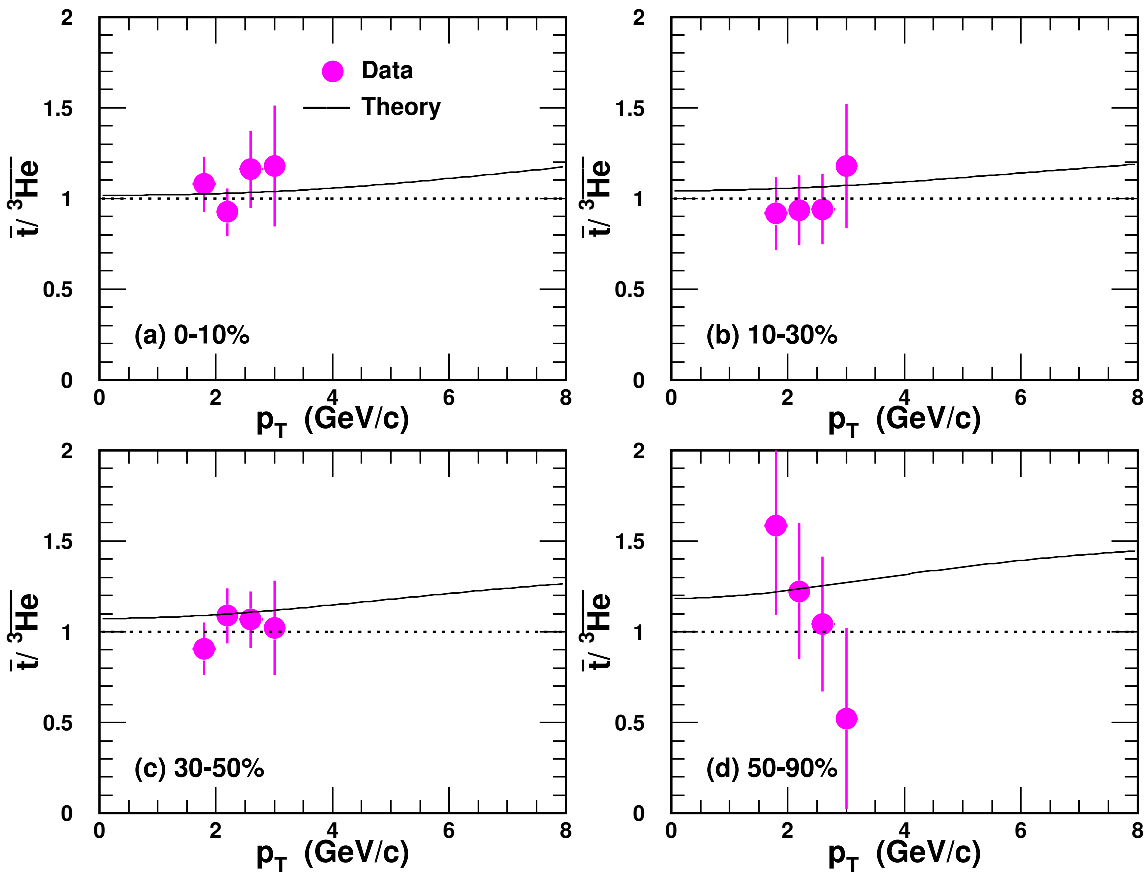

Fig. 7. Yield ratio $\bar{t}/^3\overline{\mathrm{He}}$ as a function of p_T in different centralities in Pb+Pb collisions at $\sqrt{s_{NN}} = 5.02$ TeV. Filled circles with error bars are experimental data [30] and solid lines are theoretical results.

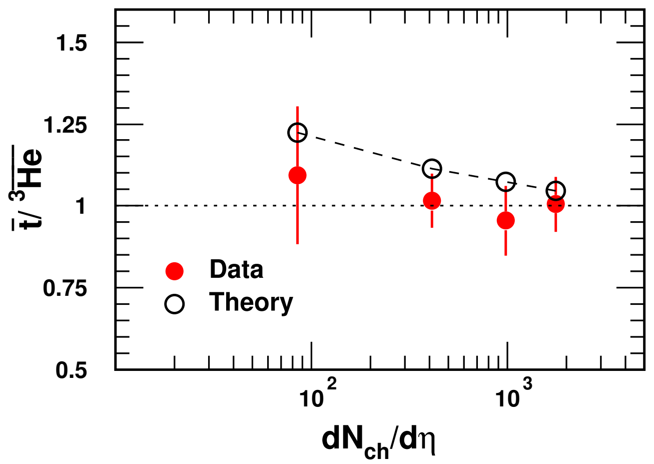

Fig. 8. Yield ratio $\bar{t}/^3\overline{\mathrm{He}}$ as a function of $dN_{ch}/d\eta$ in Pb+Pb collisions at $\sqrt{s_{NN}} = 5.02$ TeV. Filled circles with error bars are experimental data [30] and open circles connected with dashed lines to guide the eye are theoretical results.

Table 2. Values of parameters in the blast-wave model for Λ and Ω^- in different centralities in Pb+Pb collisions at $\sqrt{s_{NN}} = 5.02$ TeV.

	Centrality	T_{kin} (GeV)	$\langle\beta_T\rangle$	n
	$0-10\%$	0.090	0.670	0.64
Λ	$10-30\%$	0.092	0.648	0.70
	$30-50\%$	0.095	0.622	0.78
	$0-10\%$	0.095	0.627	0.78
Ω^-	$10-30\%$	0.097	0.569	1.05
	$30-50\%$	0.100	0.549	1.15

A. The p_T spectra of Λ and Ω^- hyperons

The p_T spectra of Λ and Ω^- hyperons are necessary for computing p_T distributions of $^3_\Lambda$H and Ω-hypernuclei. We use the blast-wave model to get p_T distribution functions by fitting the experimental data of Λ and Ω^- in Pb+Pb collisions at $\sqrt{s_{NN}} = 5.02$ TeV in $0-10\%$, $10-30\%$, and $30-50\%$ centralities [84]. They are shown in Fig. 9. Filled symbols with error bars are experimental data [84], and dashed lines are the results of the blast-wave model. Values of the blast-wave fit parameters for Λ and Ω^- are in Table 2. The p_T spectra in $0-10\%$, $10-30\%$ and $30-50\%$ centralities are scaled by 2^0,

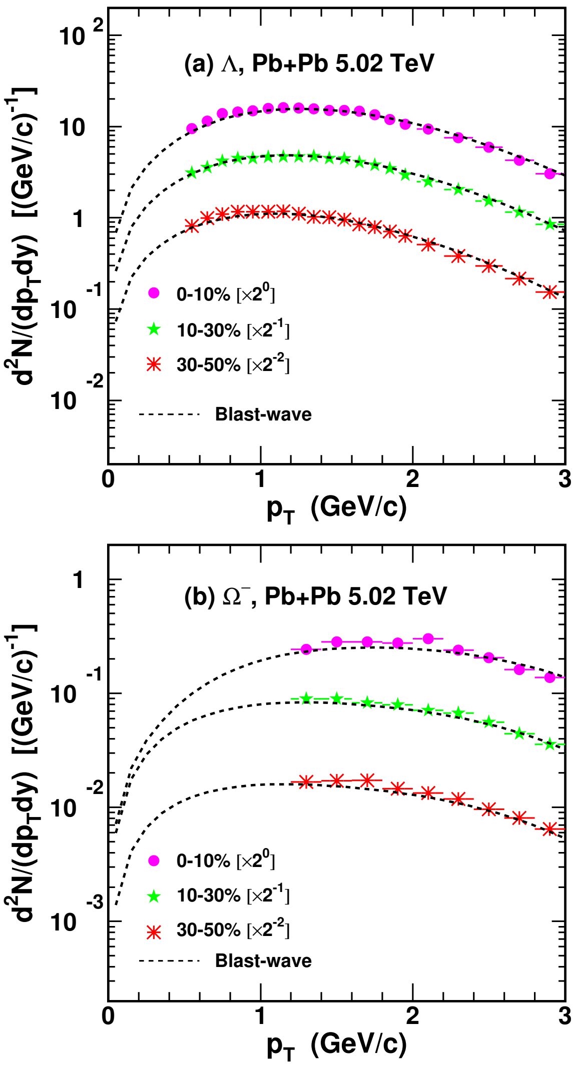

Fig. 9. The p_T spectra of (a) Λ and (b) Ω^- in different centralities in Pb+Pb collisions at $\sqrt{s_{NN}} = 5.02$ TeV. Symbols with error bars are experimental data [84] and dashed lines are the results of the blast-wave model.

2^{-1} and 2^{-2}, respectively, for clarity in the figure. We have also studied the p_T spectra of Λ and Ω^- hyperons with the Quark Combination Model developed by the Shandong group (SDQCM) in another work [85], where the results are consistent with the blast-wave model at low and intermediate p_T regions. We in the following use these Λ and Ω^- hyperons in Fig. 9 to compute productions of the ${}^3_\Lambda$H and Ω-hypernuclei. The values of parameters a and b in $R_f(p_T)$ for $H(p\Omega^-)$ and $H(n\Omega^-)$ are the same as the deuteron, and those for ${}^3_\Lambda$H and $H(pn\Omega^-)$ are the same with ^{3}He. So our calculated results for the ${}^3_\Lambda$H and Ω-hypernuclei are parameter-free, and they are more potent for further testing of the coalescence mechanism in describing the productions of nuclei with strangeness flavor quantum number.

B. The results of the ${}^3_\Lambda$H

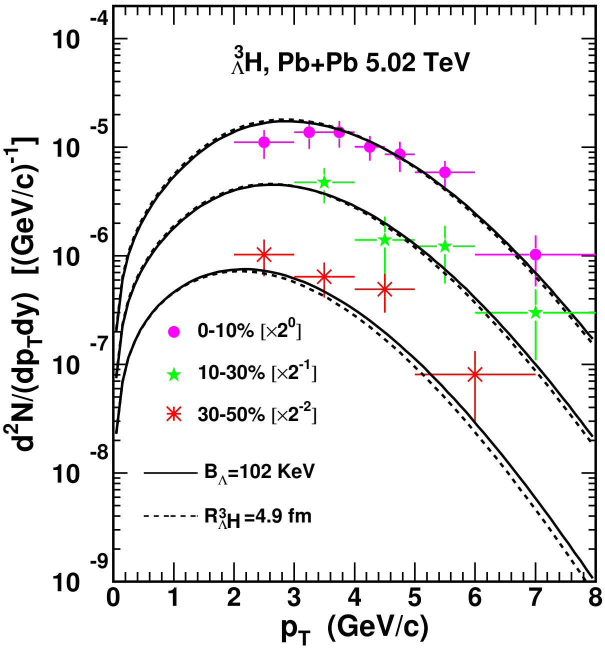

Fig. 10. The p_T spectra of the ${}^3_\Lambda$H in different centralities in Pb+Pb collisions at $\sqrt{s_{NN}} = 5.02$ TeV. Filled symbols with error bars are the experimental data [68]. The solid and dashed lines are the theoretical results with a halo structure and a spherical shape, respectively.

Based on Eq. (27), we compute the production of the ${}^3_\Lambda$H. Considering that the experimental measurements of the ${}^3_\Lambda$H suggest a halo structure with a d core encircled by a Λ, we first use $\sigma_1 = \sqrt{\frac{2(m_p+m_n)^2}{3(m_p^2+m_n^2)}} R_d$ and $\sigma_2 = \sqrt{\frac{2(m_d+m_\Lambda)^2}{9(m_d^2+m_\Lambda^2)}} r_{\Lambda d}$. The $\Lambda-d$ distance $r_{\Lambda d}$ is evaluated via $r_{\Lambda d} = \sqrt{\hbar^2/(4\mu B_\Lambda)}$ [86], where μ is the reduced mass and the binding energy B_Λ here is adopted to be the latest and most precise measurement to date 102 keV [33]. We also take a spherical shape for the ${}^3_\Lambda$H to execute the calculation to study the influence of the shape on its production. In this case, $\sigma_1 = \sqrt{\frac{m_\Lambda(m_p+m_n)(m_p+m_n+m_\Lambda)}{m_p m_n(m_p+m_n)+m_n m_\Lambda(m_n+m_\Lambda)+m_\Lambda m_p(m_\Lambda+m_p)}} R_{{}^3_\Lambda \mathrm{H}}$, $\sigma_2 = \sqrt{\frac{4 m_p m_n (m_p+m_n+m_\Lambda)^2}{3(m_p+m_n)[m_p m_n(m_p+m_n)+m_n m_\Lambda(m_n+m_\Lambda)+m_\Lambda m_p(m_\Lambda+m_p)]}} R_{{}^3_\Lambda \mathrm{H}}$, where the root-mean-square radius $R_{{}^3_\Lambda \mathrm{H}}$ is adopted to be 4.9 fm [18]. Fig. 10 shows the p_T spectra of the ${}^3_\Lambda$H in $0-10\%$, $10-30\%$ and $30-50\%$ centralities in Pb+Pb collisions at $\sqrt{s_{NN}} = 5.02$ TeV. Filled symbols with error bars are the experimental data [68]. Solid lines are the theoretical results of the coalescence model with a halo structure and dashed lines are those for a spherical shape. The p_T spectra in different centralities are scaled by different factors for clarity as shown in the figure. From Fig. 10, one can see that there exists a weak difference in the theoretical results of the p_T spectra between a halo structure and a spherical shape, and the latter gives a little softer p_T spectra. The results

with a halo structure approach to the available data better, for both amplitude and shape. This point can also be seen in the averaged transverse momenta $\langle p_T \rangle$ and yield rapidity densities dN/dy of ${}^{3}_{\Lambda}$H hereunder.

Table 3 presents $\langle p_T \rangle$ and dN/dy of ${}^{3}_{\Lambda}$H in different centralities in Pb+Pb collisions at $\sqrt{s_{NN}} = 5.02$ TeV. Experimental data in the seventh column are from Ref. [68]. Theory-4.9 in the third and eighth columns denotes theoretical results with a spherical shape at $R_{{}^{3}_{\Lambda}\mathrm{H}} = 4.9$ fm. Theory-102 in the fourth and ninth columns are theoretical results at B_Λ =102 keV. Theory-148 in the fifth and tenth columns are theoretical results at a word averaged value of B_Λ =148 keV [33]. We also give theoretical results at B_Λ =410 keV measured by the STAR collaboration [31] in the sixth and eleventh columns. Clear decreasing trends for $\langle p_T \rangle$ and dN/dy from central to semi-central collisions are observed. This is the same as light nuclei, which is due to that in more central collisions more energy is deposited in the midrapidity region and collective evolution exists longer. For the halo structure, with the increase of the B_Λ, the size of the ${}^{3}_{\Lambda}$H decreases, and the suppression effect from the ${}^{3}_{\Lambda}$H size becomes relatively weak. This leads to an increase of dN/dy with the increasing B_Λ. Besides dN/dy, such production suppression effect also affects the p_T distribution [67, 87]. This is because the suppression effect becomes stronger with a larger nucleus size in a smaller system. Recalling that $R_f(p_T)$ decreases with p_T, the ${}^{3}_{\Lambda}$H production is more suppressed in larger p_T areas in the case of larger ${}^{3}_{\Lambda}$H size. So there exists a decreasing trend for $\langle p_T \rangle$ with the decreasing B_Λ, as shown in Table 3. This is the reason why the $\langle p_T \rangle$ of ${}^{3}_{\Lambda}$H is even smaller than that of the triton while the $\langle p_T \rangle$ of Λ is larger than the nucleon.

Due to its small binding energy compared to other light (hyper-)nuclei, the ${}^{3}_{\Lambda}$H has a very loosely-bound structure and a relatively large size. It would be easily destroyed after its formation from freezeout nucleons and Λ's. As a result, the ${}^{3}_{\Lambda}$H is more likely to be produced later than the kinetic freeze-out time for the hadronic matter. In Ref. [88], the dependence of the yield of the ${}^{3}_{\Lambda}$H on its freezeout time has been studied and found the dependence is very weak. This suggests that ${}^{3}_{\Lambda}$H abundance is essentially determined when nucleons and Λ's freeze out from the system. So our coalescence calculations based on the same kinetic freezeout with light nuclei can still reasonably describe the experimental data of ${}^{3}_{\Lambda}$H.

C. Predictions of Ω-hypernuclei

The nucleon-Ω dibaryon in the S-wave and spin-2 channel is an interesting candidate for the deuteron-like state [89, 90]. The HAL QCD collaboration has reported the root-mean-square radius of $H(p\Omega^-)$ is about 3.24 fm and that of $H(n\Omega^-)$ is 3.77 fm [91]. According to Eq. (15), we study their productions, where the spin degeneracy factor $g_{H(p\Omega^-)} = g_{H(p\Omega^-)} = 5/8$. Fig. 11 shows predictions for their p_T spectra in $0-10\%$, $10-30\%$, and $30-50\%$ centralities with solid, dashed, and dash-dotted lines, respectively, in Pb+Pb collisions at $\sqrt{s_{NN}} = 5.02$ TeV. Different lines are scaled by different factors for clarity as shown in the figure.

Table 4 presents predictions of the averaged transverse momenta $\langle p_T \rangle$ and yield rapidity densities dN/dy of $H(p\Omega^-)$ and $H(n\Omega^-)$. Both of them decrease from central to semi-central collisions, similar to light nuclei and the ${}^{3}_{\Lambda}$H. The slightly lower results of $H(n\Omega^-)$ than $H(p\Omega^-)$ come from its slightly larger size.

The $H(pn\Omega^-)$ with maximal spin-$\frac{5}{2}$ is proposed to be one of the most promising partners of the t and ${}^{3}_{\Lambda}$H with multi-strangeness flavor quantum number [92]. With Eq. (27), we study its production and the spin degeneracy factor $g_{H(pn\Omega^-)} = 3/8$. As its root-mean-square radius $R_{H(pn\Omega^-)}$ is undetermined, we adopt 1.5, 2.0, and 2.5 fm to execute calculations, respectively. Fig. 12 shows predictions of the p_T spectra in $0-10\%$, $10-30\%$ and $30-50\%$ centralities in Pb+Pb collisions at $\sqrt{s_{NN}} = 5.02$ TeV. Solid, dashed, and dash-dotted lines denote results with $R_{H(pn\Omega^-)}$ =1.5, 2.0, and 2.5 fm, respectively, which are scaled by different factors for clarity as shown in the figure. Table 5 presents predictions of the averaged transverse momenta $\langle p_T \rangle$ and yield rapidity densities dN/dy of $H(pn\Omega^-)$. Theory-1.5, Theory-2.0, and Theory-2.5 denote theoretical results at $R_{H(pn\Omega^-)}$ =1.5, 2.0, and 2.5 fm, respectively.

Our predictions in central collisions for $H(p\Omega^-)$ and $H(n\Omega^-)$ are in the same magnitudes with BLWC and AMPTC models in Ref. [93], and those for $H(pn\Omega^-)$ are in the same magnitude as in Ref. [94]. Our predictions in other centralities provide more detailed references for centrality-dependent measurements of these Ω-hypernuclei in future LHC experiments.

D. Averaged transverse momentum ratios and yield ratios

Based on the results of light nuclei and hypernuclei above, we study two groups of interesting observables as powerful probes for the production correlations of different species of nuclei. One group refers to the $\langle p_T \rangle$ ratios of light nuclei to the proton and hypernuclei to hyperons. The other is their centrality-dependent yield ratios.

Fig. 13 (a) and (b) show the $\langle p_T \rangle$ ratios of dibaryon states to baryons and those of tribaryon states to baryons, i.e., $\frac{\langle p_T \rangle_d}{\langle p_T \rangle_p}$, $\frac{\langle p_T \rangle_{H(p\Omega^-)}}{\langle p_T \rangle_{\Omega^-}}$, $\frac{\langle p_T \rangle_{H(n\Omega^-)}}{\langle p_T \rangle_{\Omega^-}}$, $\frac{\langle p_T \rangle_t}{\langle p_T \rangle_p}$, $\frac{\langle p_T \rangle_{{}^3\mathrm{He}}}{\langle p_T \rangle_p}$, $\frac{\langle p_T \rangle_{{}^{3}_{\Lambda}\mathrm{H}}}{\langle p_T \rangle_\Lambda}$ and $\frac{\langle p_T \rangle_{H(pn\Omega^-)}}{\langle p_T \rangle_{\Omega^-}}$. Open symbols connected by dashed lines to guide the eye are the theoretical results of the coalescence model. All these $\langle p_T \rangle$ ratios increase as a function of $dN_{ch}/d\eta$ due to the stronger collective flow in more central collisions. More interestingly, these $\langle p_T \rangle$ ratios of light nuclei to nucleons and hypernuclei to hyperons happen to offset the $\langle p_T \rangle$ differences of p, Λ and Ω^-. This makes them more powerful to bring characteristics resulting from the production mechanism to light. Both dibaryon-to-baryon and tribaryon-to-baryon $\langle p_T \rangle$ ratios exhibit a reverse hierarchy of the nucleus sizes at any centrality, i.e., $\frac{\langle p_T \rangle_d}{\langle p_T \rangle_p} > \frac{\langle p_T \rangle_{H(p\Omega^-)}}{\langle p_T \rangle_{\Omega^-}} > \frac{\langle p_T \rangle_{H(n\Omega^-)}}{\langle p_T \rangle_{\Omega^-}}$ as $R_d < R_{H(p\Omega^-)} < R_{H(n\Omega^-)}$, and $\frac{\langle p_T \rangle_t}{\langle p_T \rangle_p} > \frac{\langle p_T \rangle_{{}^3\mathrm{He}}}{\langle p_T \rangle_p} > \frac{\langle p_T \rangle_{H(pn\Omega^-)}}{\langle p_T \rangle_{\Omega^-}} > \frac{\langle p_T \rangle_{{}^{3}_{\Lambda}\mathrm{H}}}{\langle p_T \rangle_\Lambda}$ as

Table 3. Averaged transverse momenta $\langle p_T \rangle$ and yield rapidity densities dN/dy of ${}^3_\Lambda$H in different centralities in Pb+Pb collisions at $\sqrt{s_{NN}}$ = 5.02 TeV. Experimental data in the seventh column are from Ref. [68]. Theory-4.9 denotes theoretical results with a spherical shape at $R_{{}^3_\Lambda\mathrm{H}}$ = 4.9 fm. Theory-102, Theory-148 and Theory-410 denote theoretical results with a halo structure at B_Λ =102, 148 and 410 KeV, respectively.

	Centrality	$\langle p_T \rangle$ (GeV/c)				dN/dy $(\times 10^{-5})$				
		Theory-4.9	Theory-102	Theory-148	Theory-410	Data	Theory-4.9	Theory-102	Theory-148	Theory-410
	$0-10\%$	3.16	3.19	3.24	3.37	$4.83 \pm 0.23 \pm 0.57$	6.09	5.96	7.75	12.7
${}^3_\Lambda$H	$10-30\%$	2.90	2.94	2.99	3.11	$2.62 \pm 0.25 \pm 0.40$	2.98	2.99	4.07	7.44
	$30-50\%$	2.46	2.52	2.55	2.65	$1.27 \pm 0.10 \pm 0.14$	0.875	0.932	1.35	2.94

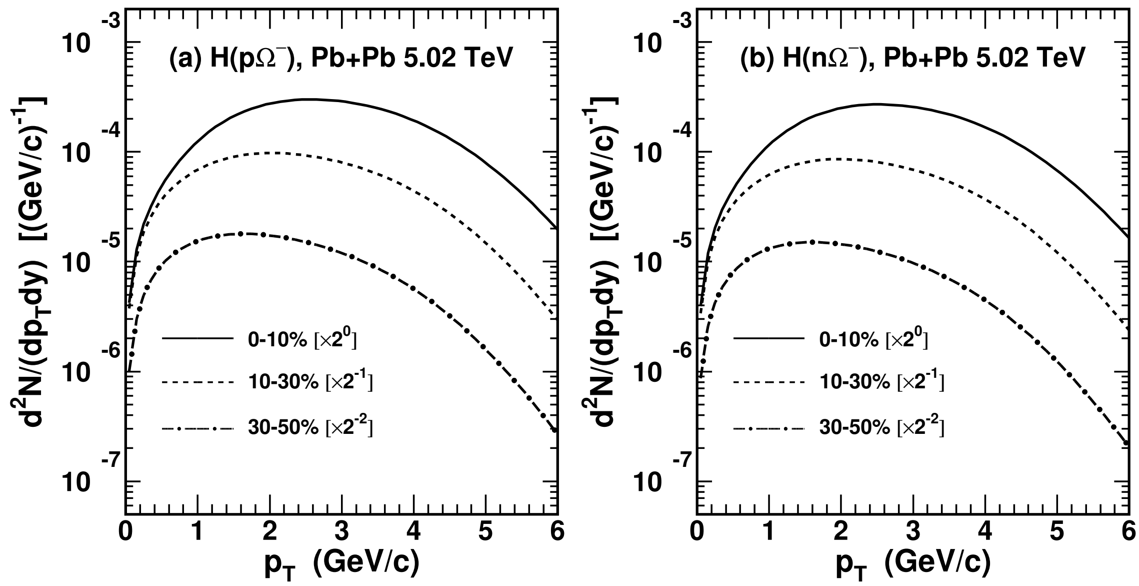

Fig. 11. Predictions of the p_T spectra of (a) $H(p\Omega^-)$ and (b) $H(n\Omega^-)$ in different centralities in Pb+Pb collisions at $\sqrt{s_{NN}} = 5.02$ TeV.

Table 4. Predictions of averaged transverse momenta $\langle p_T \rangle$ and yield rapidity densities dN/dy of $H(p\Omega^-)$ and $H(n\Omega^-)$ in different centralities in Pb+Pb collisions at $\sqrt{s_{NN}} = 5.02$ TeV.

	Centrality	$\langle p_T \rangle$ (GeV/c)	dN/dy $(\times 10^{-4})$
	$0-10\%$	2.84	9.80
$H(p\Omega^-)$	$10-30\%$	2.44	6.27
	$30-50\%$	2.18	2.16
	$0-10\%$	2.81	8.75
$H(n\Omega^-)$	$10-30\%$	2.41	5.46
	$30-50\%$	2.15	1.79

$R_t < R_{^3\mathrm{He}} < R_{H(pn\Omega^-)} < R_{{}^3_\Lambda\mathrm{H}}$. Here we take results of $H(pn\Omega^-)$ at $R_{H(pn\Omega^-)} = 2$ fm for exhibition, and those at $R_{H(pn\Omega^-)} = 1.5$, 2.5 fm give the same conclusion, a reverse hierarchy of the nucleus size. Such reverse hierarchy comes from stronger production suppression for light (hyper-) nuclei with larger sizes in higher p_T regions. This production property is very different from the thermal model in which these ratios are approximately equal to each other [47].

Fig. 13 (c) and (d) show yield ratios of dibaryon states to baryons and those of tribaryon states to baryons. Open symbols connected with dashed lines to guide the eye are the theoretical results of the coalescence model. Some of these ratios such as d/p, t/p, ^{3}He$/p$ and $H(pn\Omega^-)/\Omega^-$ decrease while the others $H(p\Omega^-)/\Omega^-$, $H(n\Omega^-)/\Omega^-$ and ${}^3_\Lambda$H$/\Lambda$ increase as a function of $dN_{ch}/d\eta$. From Eqs. (15) and (27), similar as Eq. (34), we approximately have

$$\begin{aligned} \frac{d}{p} &\sim \frac{H(p\Omega^-)}{\Omega^-} \sim \frac{H(n\Omega^-)}{\Omega^-} \\ &\propto \frac{N_p}{\langle R_f\rangle^3 \left(C_0 + \frac{\sigma^2}{\langle R_f\rangle^2}\right)\sqrt{\frac{C_0}{\langle\gamma\rangle^2} + \frac{\sigma^2}{\langle R_f\rangle^2}}} \\ &= \frac{N_p}{\langle R_f\rangle^3/\langle\gamma\rangle} \times \frac{1}{\left(C_0 + \frac{\sigma^2}{\langle R_f\rangle^2}\right)\sqrt{C_0 + \frac{\sigma^2}{\langle R_f\rangle^2/\langle\gamma\rangle^2}}}, \end{aligned} \tag{35}$$

and

$$\begin{aligned} \frac{t}{p} &\sim \frac{{}^3\mathrm{He}}{p} \sim \frac{{}^3_\Lambda\mathrm{H}}{\Lambda} \sim \frac{H(pn\Omega^-)}{\Omega^-} \\ &\propto \frac{N_p^2}{\langle R_f\rangle^6 \left(C_0 + \frac{\sigma_1^2}{\langle R_f\rangle^2}\right)\sqrt{\frac{C_0}{\langle\gamma\rangle^2} + \frac{\sigma_1^2}{\langle R_f\rangle^2}}} \end{aligned}$$

Table 5. Predictions of averaged transverse momenta $\langle p_T\rangle$ and yield rapidity densities dN/dy of $H(pn\Omega^-)$ in different centralities in Pb+Pb collisions at $\sqrt{s_{NN}} = 5.02$ TeV. Theory-1.5, Theory-2.0, and Theory-2.5 denote theoretical results at $R_{H(pn\Omega^-)}$ =1.5, 2.0, and 2.5 fm, respectively.

	Centrality	$\langle p_T\rangle$ (GeV/c)			dN/dy $(\times 10^{-6})$		
		Theory-1.5	Theory-2.0	Theory-2.5	Theory-1.5	Theory-2.0	Theory-2.5
	$0-10\%$	3.94	3.88	3.82	4.77	4.17	3.56
$H(pn\Omega^-)$	$10-30\%$	3.44	3.36	3.29	3.50	2.95	2.41
	$30-50\%$	2.98	2.89	2.81	1.60	1.24	0.92

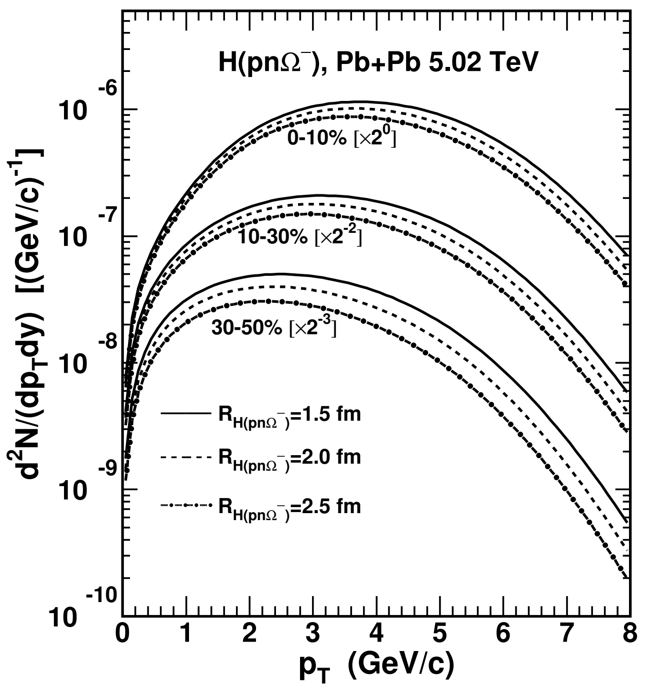

Fig. 12. Predictions of the p_T spectra of $H(pn\Omega^-)$ in different centralities in Pb+Pb collisions at $\sqrt{s_{NN}} = 5.02$ TeV.

$$\times \frac{1}{\left(\frac{4C_0}{3}+\frac{\sigma_2^2}{\langle R_f\rangle^2}\right)\sqrt{\frac{4C_0}{3\langle\gamma\rangle^2}+\frac{\sigma_2^2}{\langle R_f\rangle^2}}}$$

$$=\left(\frac{N_p}{\langle R_f\rangle^3/\langle\gamma\rangle}\right)^2 \frac{1}{\left(C_0+\frac{\sigma_1^2}{\langle R_f\rangle^2}\right)\sqrt{C_0+\frac{\sigma_1^2}{\langle R_f\rangle^2/\langle\gamma\rangle^2}}}$$

$$\times\frac{1}{\left(\frac{4C_0}{3}+\frac{\sigma_2^2}{\langle R_f\rangle^2}\right)\sqrt{\frac{4C_0}{3}+\frac{\sigma_2^2}{\langle R_f\rangle^2/\langle\gamma\rangle^2}}}. \quad (36)$$

Eqs. (35) and (36) show that behaviors of these two-particle yield ratios closely relate with the nucleon number density $\frac{N_p}{\langle R_f\rangle^3/\langle\gamma\rangle}$ and the production suppression effect items of the relative size of nuclei to hadronic source systems $\frac{\sigma}{\langle R_f\rangle}$, $\frac{\sigma_1}{\langle R_f\rangle}$ and $\frac{\sigma_2}{\langle R_f\rangle}$.

For the limit case of the nuclei with very small (negligible) sizes compared to the hadronic system scale, the $dN_{ch}/d\eta$-dependent behaviors of their yield ratios to baryons are completely determined by the nucleon number density. For the general case, the item $\frac{\sigma_i}{\langle R_f\rangle}$ suppresses these ratios and such suppression becomes weaker in larger hadronic systems. This makes these yield ratios increase from peripheral to central collisions, i.e., with the increasing $dN_{ch}/d\eta$. The larger the nucleus size, the stronger the increase as a function of $dN_{ch}/d\eta$. The nucleon density decreases with increasing $dN_{ch}/d\eta$ [80], which makes these ratios decrease. As the root-mean-square radii of d, t, ^{3}He and $H(pn\Omega^-)$ are about or smaller than 2 fm, the decreasing nucleon density dominates the behaviors of their yield ratios to baryons. But for $H(p\Omega^-)$, $H(n\Omega^-)$ and $^3_\Lambda$H, their root-mean-square radii are larger than 3 fm, the production suppression effect from their sizes becomes dominant, which leads their yield ratios to baryons increase as a function of $dN_{ch}/d\eta$. Such different centrality-dependent behaviors can help justify their own sizes of more light nuclei and hypernuclei in future experiments.

V. SUMMARY

We extended the analytical coalescence model previously developed for the productions of light nuclei to include the hyperon coalescence to simultaneously study production characteristics of d, $^3\overline{\text{He}}$, $\bar{t}$, $^3_\Lambda$H and Ω-hypernuclei. We derived the formulae of momentum distributions of two baryons coalescing into dibaryon states and three baryons coalescing into tribaryon states. The relationships of dibaryon states and tribaryon states with primordial baryons in momentum space in the laboratory frame were given. The effects of the hadronic system scale and the nucleus's own size on the nucleus production were clearly presented.

We applied the extended coalescence model to Pb+Pb collisions at $\sqrt{s_{NN}} = 5.02$ TeV. We explained the available data of B_2 and B_3, p_T spectra, averaged transverse momenta and yield rapidity densities of the d, $^3\overline{\text{He}}$, $\bar{t}$, and $^3_\Lambda$H measured by the ALICE collaboration. We provided predictions of the p_T spectra, averaged transverse momenta and yield rapidity densities of different Ω-hypernuclei, e.g., $H(p\Omega^-)$, $H(n\Omega^-)$, and $H(pn\Omega^-)$, for future experimental measurements.

More interestingly, we found two groups of novel observables. One referred to the averaged transverse momentum ratios $\frac{\langle p_T\rangle_d}{\langle p_T\rangle_p}$, $\frac{\langle p_T\rangle_{H(p\Omega^-)}}{\langle p_T\rangle_{\Omega^-}}$, $\frac{\langle p_T\rangle_{H(n\Omega^-)}}{\langle p_T\rangle_{\Omega^-}}$, $\frac{\langle p_T\rangle_t}{\langle p_T\rangle_p}$, $\frac{\langle p_T\rangle_{^3\text{He}}}{\langle p_T\rangle_p}$, $\frac{\langle p_T\rangle_{^3_\Lambda\text{H}}}{\langle p_T\rangle_\Lambda}$, and $\frac{\langle p_T\rangle_{H(pn\Omega^-)}}{\langle p_T\rangle_{\Omega^-}}$. They exhibited a reverse hierarchy according to the sizes of the nuclei themselves at any collision cen-

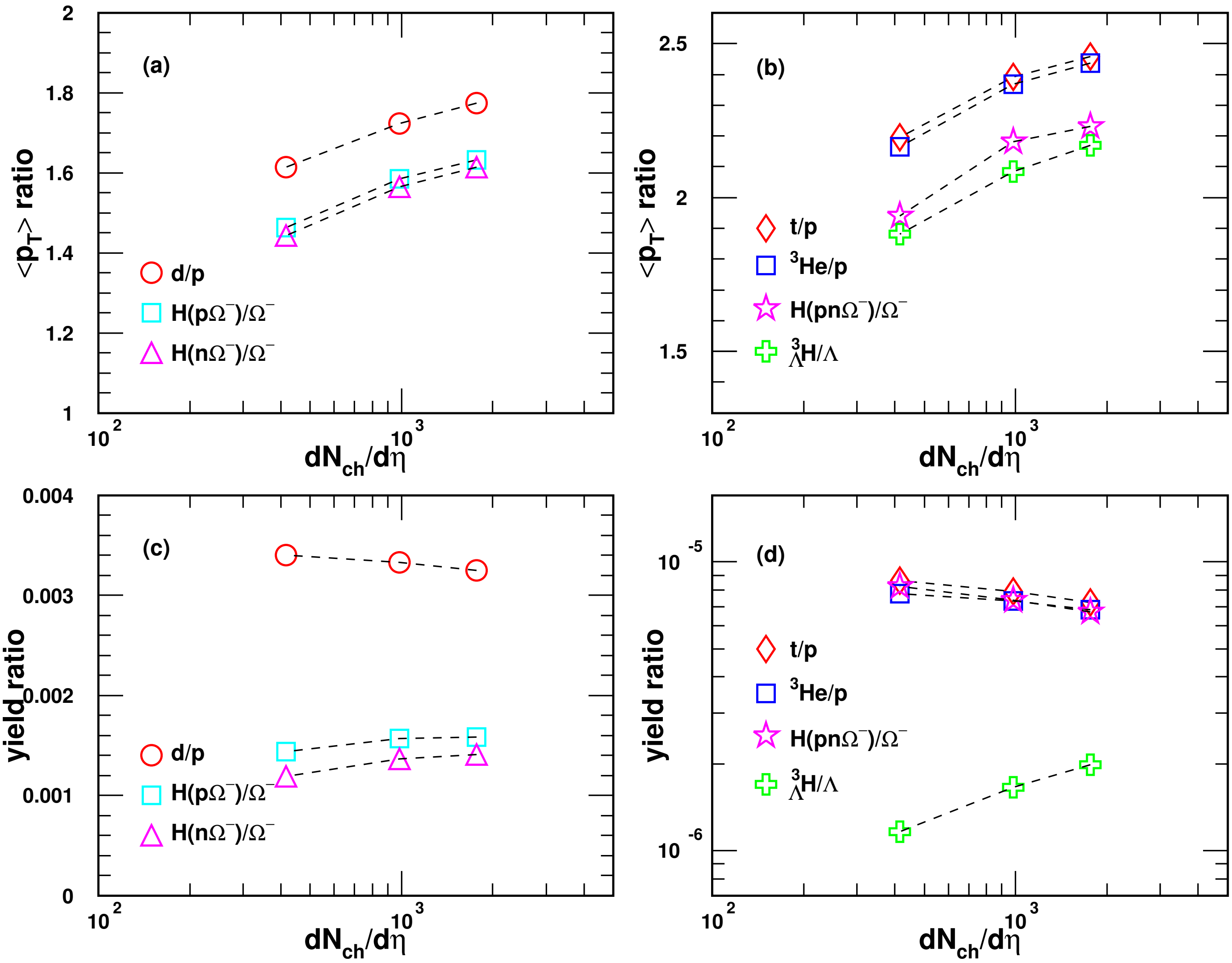

Fig. 13. The $\langle p_T \rangle$ ratios of (a) dibaryon states to baryons, (b) tribaryon states to baryons, and the yield ratios of (c) dibaryon states to baryons, (d) tribaryon states to baryons as a function of $dN_{ch}/d\eta$ in Pb+Pb collisions at $\sqrt{s_{NN}} = 5.02$ TeV. Different open symbols connected with dashed lines to guide the eye are the theoretical results.

trality. The other group involved the centrality-dependent yield ratios $\frac{d}{p}$, $\frac{H(p\Omega^-)}{\Omega^-}$, $\frac{H(n\Omega^-)}{\Omega^-}$, $\frac{t}{p}$, $\frac{^3\mathrm{He}}{p}$, $\frac{^3_\Lambda\mathrm{H}}{\Lambda}$, and $\frac{H(pn\Omega^-)}{\Omega^-}$. Some of these yield ratios $\frac{d}{p}$, $\frac{t}{p}$, $\frac{^3\mathrm{He}}{p}$ and $\frac{H(pn\Omega^-)}{\Omega^-}$ decreased while the others $\frac{H(p\Omega^-)}{\Omega^-}$, $\frac{H(n\Omega^-)}{\Omega^-}$ and $\frac{^3_\Lambda\mathrm{H}}{\Lambda}$ increased as a function of $dN_{ch}/d\eta$. Such different trends were caused by different production suppression degrees from the nucleus sizes. The behaviors of these two groups of ratios in the coalescence mechanism were different from the thermal model. They were powerful observables for probing the production mechanism of light (hyper-)nuclei. They unfolded the production relations of different sorts of nuclei in the coalescence frame.

---

[1] J. Aichelin, 'Quantum' molecular dynamics: A Dynamical microscopic n body approach to investigate fragment formation and the nuclear equation of state in heavy ion collisions. Phys. Rept. **202**, 233–360 (1991). doi:10.1016/0370-1573(91)90094-3

[2] K.J. Sun, R. Wang, C.M. Ko et al., Unveiling the dynamics of little-bang nucleosynthesis. Nature Commun. **15**, 1074 (2024). arXiv:2207.12532, doi:10.1038/s41467-024-45474-x

[3] A. Andronic, P. Braun-Munzinger, K. Redlich et al., Decoding the phase structure of QCD via particle production at high energy. Nature **561**, 321–330 (2018). arXiv:1710.09425, doi:10.1038/s41586-018-0491-6

[4] K.J. Sun, L.W. Chen, C.M. Ko et al., Probing QCD critical fluctuations from light nuclei production in relativistic

heavy-ion collisions. Phys. Lett. B **774**, 103–107 (2017). arXiv:1702.07620, doi:10.1016/j.physletb.2017.09.056

[5] K.J. Sun, L.W. Chen, C.M. Ko et al., Light nuclei production as a probe of the QCD phase diagram. Phys. Lett. B **781**, 499–504 (2018). arXiv:1801.09382, doi:10.1016/j.physletb.2018.04.035

[6] A. Bzdak, S. Esumi, V. Koch et al., Mapping the Phases of Quantum Chromodynamics with Beam Energy Scan. Phys. Rept. **853**, 1–87 (2020). arXiv:1906.00936, doi:10.1016/j.physrep.2020.01.005

[7] X. Luo, S. Shi, N. Xu et al., A Study of the Properties of the QCD Phase Diagram in High-Energy Nuclear Collisions. Particles **3**, 278–307 (2020). arXiv:2004.00789, doi:10.3390/particles3020022

[8] H. Liu, D. Zhang, S. He et al., Light nuclei production in Au+Au collisions at sNN = 5–200 GeV from JAM model. Phys. Lett. B **805**, 135452 (2020). [Erratum: Phys.Lett.B 829, 137132 (2022)]. arXiv:1909.09304, doi:10.1016/j.physletb.2020.135452

[9] J. Steinheimer, M. Mitrovski, T. Schuster et al., Strangeness fluctuations and MEMO production at FAIR. Phys. Lett. B **676**, 126–131 (2009). arXiv:0811.4077, doi:10.1016/j.physletb.2009.04.062

[10] T. Shao, J. Chen, C.M. Ko et al., Yield ratio of hypertriton to light nuclei in heavy-ion collisions from $\sqrt{s_{\rm NN}}$ = 4.9 GeV to 2.76 TeV. Chin. Phys. C **44**, 114001 (2020). arXiv:2004.02385, doi:10.1088/1674-1137/abadf0

[11] J.L. Nagle, B.S. Kumar, M.J. Bennett et al., Source size determination in relativistic nucleus-nucleus collisions. Phys. Rev. Lett. **73**, 1219–1222 (1994). doi:10.1103/PhysRevLett.73.1219

[12] J. Chen, D. Keane, Y.G. Ma et al., Antinuclei in Heavy-Ion Collisions. Phys. Rept. **760**, 1–39 (2018). arXiv:1808.09619, doi:10.1016/j.physrep.2018.07.002

[13] K. Blum, M. Takimoto, Nuclear coalescence from correlation functions. Phys. Rev. C **99**, 044913 (2019). arXiv:1901.07088, doi:10.1103/PhysRevC.99.044913

[14] S. Bazak, S. Mrowczynski, Production of ^{4}Li and $p-{}^3$He correlation function in relativistic heavy-ion collisions. Eur. Phys. J. A **56**, 193 (2020). arXiv:2001.11351, doi:10.1140/epja/s10050-020-00198-6

[15] H.H. Gutbrod, A. Sandoval, P.J. Johansen et al., Final State Interactions in the Production of Hydrogen and Helium Isotopes by Relativistic Heavy Ions on Uranium. Phys. Rev. Lett. **37**, 667–670 (1976). doi:10.1103/PhysRevLett.37.667

[16] Y.X. Zhang, S. Zhang, Y.G. Ma, Deuteron production mechanism via azimuthal correlation for $p-p$ and p-Pb collisions at LHC energy with the AMPT model. Eur. Phys. J. A **59**, 72 (2023). doi:10.1140/epja/s10050-023-00980-2

[17] S.R. Beane, E. Chang, S.D. Cohen et al., Light Nuclei and Hypernuclei from Quantum Chromodynamics in the Limit of SU(3) Flavor Symmetry. Phys. Rev. D **87**, 034506 (2013). arXiv:1206.5219, doi:10.1103/PhysRevD.87.034506

[18] H. Nemura, Y. Suzuki, Y. Fujiwara et al., Study of light Lambda and Lambda-Lambda hypernuclei with the stochastic variational method and effective Lambda N potentials. Prog. Theor. Phys. **103**, 929–958 (2000). arXiv:nucl-th/9912065, doi:10.1143/PTP.103.929

[19] Y.G. Ma, Hypernuclei as a laboratory to test hyperon-nucleon interactions. Nucl. Sci. Tech. **34**, 97 (2023). doi:10.1007/s41365-023-01248-6

[20] P. Junnarkar, N. Mathur, Deuteronlike Heavy Dibaryons from Lattice Quantum Chromodynamics. Phys. Rev. Lett. **123**, 162003 (2019). arXiv:1906.06054, doi:10.1103/PhysRevLett.123.162003

[21] K. Morita, S. Gongyo, T. Hatsuda et al., Probing $\Omega\Omega$ and $p\Omega$ dibaryons with femtoscopic correlations in relativistic heavy-ion collisions. Phys. Rev. C **101**, 015201 (2020). arXiv:1908.05414, doi:10.1103/PhysRevC.101.015201

[22] S. Afanasiev et al., Elliptic flow for phi mesons and (anti)deuterons in Au + Au collisions at s(NN)**(1/2) = 200-GeV. Phys. Rev. Lett. **99**, 052301 (2007). arXiv:nucl-ex/0703024, doi:10.1103/PhysRevLett.99.052301

[23] T. Anticic et al., Production of deuterium, tritium, and He3 in central Pb + Pb collisions at 20A,30A,40A,80A , and 158A GeV at the CERN Super Proton Synchrotron. Phys. Rev. C **94**, 044906 (2016). arXiv:1606.04234, doi:10.1103/PhysRevC.94.044906

[24] C. Adler et al., Anti-deuteron and anti-He-3 production in s(NN)**(1/2) = 130-GeV Au+Au collisions. Phys. Rev. Lett. **87**, 262301 (2001). [Erratum: Phys.Rev.Lett. 87, 279902 (2001)]. arXiv:nucl-ex/0108022, doi:10.1103/PhysRevLett.87.262301

[25] L. Adamczyk et al., Measurement of elliptic flow of light nuclei at $\sqrt{s_{NN}}$ = 200, 62.4, 39, 27, 19.6, 11.5, and 7.7 GeV at the BNL Relativistic Heavy Ion Collider. Phys. Rev. C **94**, 034908 (2016). arXiv:1601.07052, doi:10.1103/PhysRevC.94.034908

[26] J. Adam et al., Beam-energy dependence of the directed flow of deuterons in Au+Au collisions. Phys. Rev. C **102**, 044906 (2020). arXiv:2007.04609, doi:10.1103/PhysRevC.102.044906

[27] J. Adam et al., Beam energy dependence of (anti-)deuteron production in Au + Au collisions at the BNL Relativistic Heavy Ion Collider. Phys. Rev. C **99**, 064905 (2019). arXiv:1903.11778, doi:10.1103/PhysRevC.99.064905

[28] M. Abdulhamid et al., Beam Energy Dependence of Triton Production and Yield Ratio ($\mathrm{N}_t \times \mathrm{N}_p/\mathrm{N}_d^2$) in Au+Au Collisions at RHIC. Phys. Rev. Lett. **130**, 202301 (2023). arXiv:2209.08058, doi:10.1103/PhysRevLett.130.202301

[29] S. Acharya et al., Elliptic and triangular flow of (anti)deuterons in Pb-Pb collisions at $\sqrt{s_{\rm NN}}$ = 5.02 TeV. Phys. Rev. C **102**, 055203 (2020). arXiv:2005.14639, doi:10.1103/PhysRevC.102.055203

[30] S. Acharya et al., Light (anti)nuclei production in Pb-Pb collisions at sNN=5.02 TeV. Phys. Rev. C **107**, 064904 (2023). arXiv:2211.14015, doi:10.1103/PhysRevC.107.064904

[31] J. Adam et al., Measurement of the mass difference and the binding energy of the hypertriton and antihypertriton. Nature Phys. **16**, 409–412 (2020). arXiv:1904.10520, doi:10.1038/s41567-020-0799-7

[32] M. Abdallah et al., Measurements of H^3_Λ and H^4_Λ Lifetimes and Yields in Au+Au Collisions in the High Baryon Density Region. Phys. Rev. Lett. **128**, 202301 (2022). arXiv:2110.09513, doi:10.1103/PhysRevLett.128.202301

[33] S. Acharya et al., Measurement of the Lifetime and Λ Separation Energy of HΛ3. Phys. Rev. Lett. **131**, 102302 (2023). arXiv:2209.07360, doi:10.1103/PhysRevLett.131.102302

[34] J. Adam et al., ${}^3_\Lambda$H and ${}^3_{\bar{\Lambda}}\overline{\mathrm{H}}$ production in Pb-Pb collisions at $\sqrt{s_{\rm NN}}$ = 2.76 TeV. Phys. Lett. B **754**, 360–372 (2016). arXiv:1506.08453, doi:10.1016/j.physletb.2016.01.040

[35] J. Chen et al., Properties of the QCD matter: review of selected results from the relativistic heavy ion collider beam energy scan (RHIC BES) program. Nucl. Sci. Tech. **35**, 214 (2024). arXiv:2407.02935, doi:10.1007/s41365-024-01591-2

[36] P. Braun-Munzinger, B. Dönigus, Loosely-bound objects produced in nuclear collisions at the LHC. Nucl. Phys. A **987**, 144–201 (2019). arXiv:1809.04681,

doi:10.1016/j.nuclphysa.2019.02.006
[37] D. Oliinychenko, Overview of light nuclei production in relativistic heavy-ion collisions. Nucl. Phys. A **1005**, 121754 (2021). arXiv:2003.05476, doi:10.1016/j.nuclphysa.2020.121754
[38] S. Mrowczynski, Production of light nuclei at colliders – coalescence vs. thermal model. Eur. Phys. J. ST **229**, 3559–3583 (2020). arXiv:2004.07029, doi:10.1140/epjst/e2020-000067-0
[39] B. Dönigus, G. Röpke, D. Blaschke, Deuteron yields from heavy-ion collisions at energies available at the CERN Large Hadron Collider: Continuum correlations and in-medium effects. Phys. Rev. C **106**, 044908 (2022). arXiv:2206.10376, doi:10.1103/PhysRevC.106.044908
[40] C.B. Dover, U.W. Heinz, E. Schnedermann et al., Relativistic coalescence model for high-energy nuclear collisions. Phys. Rev. C **44**, 1636–1654 (1991). doi:10.1103/PhysRevC.44.1636
[41] L.W. Chen, C.M. Ko, B.A. Li, Light clusters production as a probe to the nuclear symmetry energy. Phys. Rev. C **68**, 017601 (2003). arXiv:nucl-th/0302068, doi:10.1103/PhysRevC.68.017601
[42] P. Liu, J.H. Chen, Y.G. Ma et al., Production of light nuclei and hypernuclei at High Intensity Accelerator Facility energy region. Nucl. Sci. Tech. **28**, 55 (2017). [Erratum: Nucl.Sci.Tech. 28, 89 (2017)]. doi:10.1007/s41365-017-0207-x
[43] L.L. Zhu, B. Wang, M. Wang et al., Energy and centrality dependence of light nuclei production in relativistic heavy-ion collisions. Nucl. Sci. Tech. **33**, 45 (2022). doi:10.1007/s41365-022-01028-8
[44] K.J. Sun, C.M. Ko, Event-by-event antideuteron multiplicity fluctuation in Pb+Pb collisions at sNN=5.02 TeV. Phys. Lett. B **840**, 137864 (2023). arXiv:2204.10879, doi:10.1016/j.physletb.2023.137864
[45] R. Wang, Y.G. Ma, L.W. Chen et al., Kinetic approach of light-nuclei production in intermediate-energy heavy-ion collisions. Phys. Rev. C **108**, L031601 (2023). arXiv:2305.02988, doi:10.1103/PhysRevC.108.L031601
[46] F. Li, S. Zhang, K.J. Sun et al., Production of light nuclei in isobaric Ru + Ru and Zr + Zr collisions at sNN=7.7–200 GeV from a multiphase transport model. Phys. Rev. C **109**, 064912 (2024). arXiv:2405.11558, doi:10.1103/PhysRevC.109.064912
[47] A. Andronic, P. Braun-Munzinger, J. Stachel et al., Production of light nuclei, hypernuclei and their antiparticles in relativistic nuclear collisions. Phys. Lett. B **697**, 203–207 (2011). arXiv:1010.2995, doi:10.1016/j.physletb.2011.01.053
[48] A. Mekjian, Thermodynamic Model for Composite Particle Emission in Relativistic Heavy Ion Collisions. Phys. Rev. Lett. **38**, 640–643 (1977). doi:10.1103/PhysRevLett.38.640
[49] P.J. Siemens, J.I. Kapusta, EVIDENCE FOR A SOFT NUCLEAR MATTER EQUATION OF STATE. Phys. Rev. Lett. **43**, 1486–1489 (1979). doi:10.1103/PhysRevLett.43.1486
[50] J. Cleymans, S. Kabana, I. Kraus et al., Antimatter production in proton-proton and heavy-ion collisions at ultrarelativistic energies. Phys. Rev. C **84**, 054916 (2011). arXiv:1105.3719, doi:10.1103/PhysRevC.84.054916
[51] Y. Cai, T.D. Cohen, B.A. Gelman et al., Yields of weakly-bound light nuclei as a probe of the statistical hadronization model. Phys. Rev. C **100**, 024911 (2019). arXiv:1905.02753, doi:10.1103/PhysRevC.100.024911
[52] A. Schwarzschild, C. Zupancic, Production of Tritons, Deuterons, Nucleons, and Mesons by 30-GeV Protons on A-1, Be, and Fe Targets. Phys. Rev. **129**, 854–862 (1963). doi:10.1103/PhysRev.129.854
[53] H. Sato, K. Yazaki, On the coalescence model for high-energy nuclear reactions. Phys. Lett. B **98**, 153–157 (1981). doi:10.1016/0370-2693(81)90976-X
[54] R. Mattiello, A. Jahns, H. Sorge et al., Deuteron flow in ultra-relativistic heavy ion reactions. Phys. Rev. Lett. **74**, 2180–2183 (1995). doi:10.1103/PhysRevLett.74.2180
[55] J.L. Nagle, B.S. Kumar, D. Kusnezov et al., Coalescence of deuterons in relativistic heavy ion collisions. Phys. Rev. C **53**, 367–376 (1996). doi:10.1103/PhysRevC.53.367
[56] R. Mattiello, H. Sorge, H. Stocker et al., Nuclear clusters as a probe for expansion flow in heavy ion reactions at 10-A/GeV - 15-A/GeV. Phys. Rev. C **55**, 1443–1454 (1997). arXiv:nucl-th/9607003, doi:10.1103/PhysRevC.55.1443
[57] A. Polleri, J.P. Bondorf, I.N. Mishustin, Effects of collective expansion on light cluster spectra in relativistic heavy ion collisions. Phys. Lett. B **419**, 19–24 (1998). arXiv:nucl-th/9711011, doi:10.1016/S0370-2693(97)01455-X
[58] N. Sharma, T. Perez, A. Castro et al., Methods for separation of deuterons produced in the medium and in jets in high energy collisions. Phys. Rev. C **98**, 014914 (2018). arXiv:1803.02313, doi:10.1103/PhysRevC.98.014914
[59] R. Scheibl, U.W. Heinz, Coalescence and flow in ultrarelativistic heavy ion collisions. Phys. Rev. C **59**, 1585–1602 (1999). arXiv:nucl-th/9809092, doi:10.1103/PhysRevC.59.1585
[60] W. Zhao, L. Zhu, H. Zheng et al., Spectra and flow of light nuclei in relativistic heavy ion collisions at energies available at the BNL Relativistic Heavy Ion Collider and at the CERN Large Hadron Collider. Phys. Rev. C **98**, 054905 (2018). arXiv:1807.02813, doi:10.1103/PhysRevC.98.054905
[61] Y.H. Feng, C.M. Ko, Y.G. Ma et al., Jet-induced enhancement of deuteron production in pp and p-Pb collisions at the LHC. Phys. Lett. B **859**, 139102 (2024). arXiv:2408.01634, doi:10.1016/j.physletb.2024.139102
[62] T.T. Wang, Y.G. Ma, Nucleon-number scalings of anisotropic flows and nuclear modification factor for light nuclei in the squeeze-out region. Eur. Phys. J. A **55**, 102 (2019). arXiv:2002.06067, doi:10.1140/epja/i2019-12788-0
[63] W. Zhao, K.j. Sun, C.M. Ko et al., Multiplicity scaling of light nuclei production in relativistic heavy-ion collisions. Phys. Lett. B **820**, 136571 (2021). arXiv:2105.14204, doi:10.1016/j.physletb.2021.136571
[64] X.Y. Zhao, Y.T. Feng, F.L. Shao et al., Production characteristics of light (anti-)nuclei from (anti-)nucleon coalescence in heavy ion collisions at energies employed at the RHIC beam energy scan. Phys. Rev. C **105**, 054908 (2022). arXiv:2201.10354, doi:10.1103/PhysRevC.105.054908
[65] R.Q. Wang, J.P. Lv, Y.H. Li et al., Different coalescence sources of light nucleus production in Au-Au collisions at GeV*. Chin. Phys. C **48**, 053112 (2024). arXiv:2210.10271, doi:10.1088/1674-1137/ad2b56
[66] R.Q. Wang, F.L. Shao, J. Song, Momentum dependence of light nuclei production in $p-p$, $p-Pb$, and Pb-Pb collisions at energies available at the CERN Large Hadron Collider. Phys. Rev. C **103**, 064908 (2021). arXiv:2007.05745, doi:10.1103/PhysRevC.103.064908
[67] R.Q. Wang, Y.H. Li, J. Song et al., Production properties of deuterons, tritons, and He3 via an analytical nucleon coalescence method in Pb-Pb collisions at sNN=2.76TeV. Phys. Rev. C **109**, 034907 (2024). arXiv:2309.16296, doi:10.1103/PhysRevC.109.034907
[68] S. Acharya et al., Measurement of ${}^{3}_{\Lambda}$H production in Pb-Pb collisions at $\sqrt{s_{\mathrm{NN}}} = 5.02$ TeV. . arXiv:2405.19839
[69] L.W. Chen, C.M. Ko, B.A. Li, Light cluster production in

intermediate-energy heavy ion collisions induced by neutron rich nuclei. Nucl. Phys. A **729**, 809–834 (2003). arXiv:nucl-th/0306032, doi:10.1016/j.nuclphysa.2003.09.010

[70] C.M. Ko, T. Song, F. Li et al., Partonic mean-field effects on matter and antimatter elliptic flows. Nucl. Phys. A **928**, 234–246 (2014). arXiv:1211.5511, doi:10.1016/j.nuclphysa.2014.05.016

[71] L. Zhu, C.M. Ko, X. Yin, Light (anti-)nuclei production and flow in relativistic heavy-ion collisions. Phys. Rev. C **92**, 064911 (2015). arXiv:1510.03568, doi:10.1103/PhysRevC.92.064911

[72] S. Mrowczynski, Production of light nuclei in the thermal and coalescence models. Acta Phys. Polon. B **48**, 707 (2017). arXiv:1607.02267, doi:10.5506/APhysPolB.48.707

[73] A. Kisiel, M. Gałażyn, P. Bożek, Pion, kaon, and proton femtoscopy in Pb–Pb collisions at $\sqrt{s_{\rm NN}}$=2.76 TeV modeled in (3+1)D hydrodynamics. Phys. Rev. C **90**, 064914 (2014). arXiv:1409.4571, doi:10.1103/PhysRevC.90.064914

[74] J. Adam et al., Centrality dependence of pion freeze-out radii in Pb-Pb collisions at $\sqrt{s_{NN}}$ = 2.76 TeV. Phys. Rev. C **93**, 024905 (2016). arXiv:1507.06842, doi:10.1103/PhysRevC.93.024905

[75] Y.L. Cheng, S. Zhang, Y.G. Ma, Collision centrality and system size dependences of light nuclei production via dynamical coalescence mechanism. Eur. Phys. J. A **57**, 330 (2021). arXiv:2112.03520, doi:10.1140/epja/s10050-021-00639-w

[76] I. Angeli, K.P. Marinova, Table of experimental nuclear ground state charge radii: An update. Atom. Data Nucl. Data Tabl. **99**, 69–95 (2013). doi:10.1016/j.adt.2011.12.006

[77] M. Puccio, CERN-THESIS-2017-338. Ph.D. thesis, Turin U. (2017)

[78] P. Chakraborty, A.K. Pandey, S. Dash, Identical-particle (pion and kaon) femtoscopy in Pb–Pb collisions at $\sqrt{s_{\rm NN}}$ = 5.02 TeV with Therminator 2 modeled with (3+1)D viscous hydrodynamics. Eur. Phys. J. A **57**, 338 (2021). arXiv:2010.12161, doi:10.1140/epja/s10050-021-00647-w

[79] J. Adams et al., Pion interferometry in Au+Au collisions at S(NN)**(1/2) = 200-GeV. Phys. Rev. C **71**, 044906 (2005). arXiv:nucl-ex/0411036, doi:10.1103/PhysRevC.71.044906

[80] S. Acharya et al., Production of charged pions, kaons, and (anti-)protons in Pb-Pb and inelastic pp collisions at $\sqrt{s_{NN}}$ = 5.02 TeV. Phys. Rev. C **101**, 044907 (2020). arXiv:1910.07678, doi:10.1103/PhysRevC.101.044907

[81] E. Schnedermann, J. Sollfrank, U.W. Heinz, Thermal phenomenology of hadrons from 200-A/GeV S+S collisions. Phys. Rev. C **48**, 2462–2475 (1993). arXiv:nucl-th/9307020, doi:10.1103/PhysRevC.48.2462

[82] J. Adam et al., Production of light nuclei and anti-nuclei in pp and Pb-Pb collisions at energies available at the CERN Large Hadron Collider. Phys. Rev. C **93**, 024917 (2016). arXiv:1506.08951, doi:10.1103/PhysRevC.93.024917

[83] K.J. Sun, C.M. Ko, B. Dönigus, Suppression of light nuclei production in collisions of small systems at the Large Hadron Collider. Phys. Lett. B **792**, 132–137 (2019). arXiv:1812.05175, doi:10.1016/j.physletb.2019.03.033

[84] P. Kalinak, Strangeness production in Pb-Pb collisions with ALICE at the LHC. PoS EPS-HEP **2017**, 168 (2017). doi:10.22323/1.314.0168

[85] W.b. Chang, R.q. Wang, J. Song et al., Production of Strange and Charm Hadrons in Pb+Pb Collisions at sNN = 5.02 TeV †. Symmetry **15**, 400 (2023). arXiv:2302.07546, doi:10.3390/sym15020400

[86] C.A. Bertulani, Probing the size and binding energy of the hypertriton in heavy ion collisions. Phys. Lett. B **837**, 137639 (2023). arXiv:2211.12643, doi:10.1016/j.physletb.2022.137639

[87] D.N. Liu, C.M. Ko, Y.G. Ma et al., Softening of the hypertriton transverse momentum spectrum in heavy-ion collisions. Phys. Lett. B **855**, 138855 (2024). arXiv:2404.02701, doi:10.1016/j.physletb.2024.138855

[88] Z. Zhang, C.M. Ko, Hypertriton production in relativistic heavy ion collisions. Phys. Lett. B **780**, 191–195 (2018). doi:10.1016/j.physletb.2018.03.003

[89] H. Clement, On the History of Dibaryons and their Final Observation. Prog. Part. Nucl. Phys. **93**, 195 (2017). arXiv:1610.05591, doi:10.1016/j.ppnp.2016.12.004

[90] J. Pu, K.J. Sun, C.W. Ma et al., Probing the internal structures of pΩ and $\Omega\Omega$ with their production at the Large Hadron Collider. Phys. Rev. C **110**, 024908 (2024). arXiv:2402.04185, doi:10.1103/PhysRevC.110.024908

[91] T. Iritani et al., $N\Omega$ dibaryon from lattice QCD near the physical point. Phys. Lett. B **792**, 284–289 (2019). arXiv:1810.03416, doi:10.1016/j.physletb.2019.03.050

[92] H. Garcilazo, A. Valcarce, ΩNN and $\Omega\Omega N$ states. Phys. Rev. C **99**, 014001 (2019). arXiv:1901.05678, doi:10.1103/PhysRevC.99.014001

[93] S. Zhang, Y.G. Ma, Ω-dibaryon production with hadron interaction potential from the lattice QCD in relativistic heavy-ion collisions. Phys. Lett. B **811**, 135867 (2020). arXiv:2007.11170, doi:10.1016/j.physletb.2020.135867

[94] L. Zhang, S. Zhang, Y.G. Ma, Production of ΩNN and $\Omega\Omega N$ in ultra-relativistic heavy-ion collisions. Eur. Phys. J. C **82**, 416 (2022). arXiv:2112.02766, doi:10.1140/epjc/s10052-022-10336-7